



# Computational Fluid Dynamic Analyses for the High-Lift Common Research Model Using the USM3D and FUN3D Flow Solvers

Melissa Rivers<sup>1</sup>, Craig Hunter,<sup>2</sup> and Veer Vatsa<sup>3</sup>  
*NASA Langley Research Center, Hampton, VA 23681*

**Two Navier-Stokes codes were used to compute flow over the High-Lift Common Research Model (HL-CRM) in preparation for a wind tunnel test to be performed at the NASA Langley Research Center 14-by-22-Foot Subsonic Tunnel in fiscal year 2018. Both flight and wind tunnel conditions were simulated by the two codes at set Mach numbers and Reynolds numbers over a full angle-of-attack range for three configurations: cruise, landing and takeoff. Force curves, drag polars and surface pressure contour comparisons are shown for the two codes. The lift and drag curves compare well for the cruise configuration up to 10° angle of attack but not as well for the other two configurations. The drag polars compare reasonably well for all three configurations. The surface pressure contours compare well for some of the conditions modeled but not as well for others.**

## Nomenclature

$C_D$	=	drag coefficient
$C_L$	=	lift coefficient
$C_p$	=	pressure coefficient
$M$	=	Mach number
$Re$	=	Reynolds number
$y$	=	spanwise coordinates on a wing
$y^+$	=	normalized wall distance
$\alpha$	=	angle of attack, degrees

## I. Introduction

Accessibility to relevant commercial transport high-lift configurations in the public domain is very limited due to company data being restricted for various reasons. Because of this, the geometries that are available are either outdated or the platform is not representative of a relevant commercial transport. In an effort to alleviate this issue, a study was performed by Lacy and Sclafani<sup>1</sup> to design a set of relevant commercial transport high-lift configurations that can be used in the public domain. This previous study also sought to serve as a high-lift technology development platform and to do this while creating a geometry that was simple and easy to use. With a high-speed geometry that does not have many surfaces, the ease of use of the geometry is not generally an issue. On a high-lift geometry, however, there are many more surfaces present, which makes the geometry more challenging to use for Computational Fluid Dynamics (CFD) grid generation and to build a model for wind tunnel testing. The logical place to start designing high-lift geometries was from the previously released cruise speed Common Research Model (CRM) definition<sup>2,3</sup> as it is a wing/body/nacelle/pylon/horizontal tail geometry set representative of

<sup>1</sup> Research Engineer, Configuration Aerodynamics Branch, Mail Stop 267, AIAA Senior Member.

<sup>2</sup> Research Engineer, Configuration Aerodynamics Branch, Mail Stop 499.

<sup>3</sup> Senior Research Scientist, Computational Aerosciences Branch, Mail Stop 128, AIAA Associate Fellow.

a generic long range, twin engine transport aircraft configuration. Each component of the cruise geometry was re-evaluated for its suitability for a high-lift geometry set. The ultimate goal was to create a configuration that is representative of a modern commercial airplane.

The result of the previous study was the generation of three configurations representative of cruise, landing and takeoff configurations. The present study uses these conventional HL-CRM geometries to provide baseline data that will eventually be compared with active flow control enabled HL-CRM configurations with a simple hinge flap for both aerodynamic and acoustic research and development (R&D) efforts that cover both flight and wind tunnel Reynolds numbers (the previous study by Lacy and Sclafani only covered the flight Re). In addition, the current work may help in the model design process, such as placement of instrumentation and bracket design, and may contribute to the ongoing CFD high-lift prediction workshop. To this end, all three configurations were run at flight and wind tunnel conditions using two different unstructured CFD codes, USM3D<sup>4-7</sup> and FUN3D<sup>8</sup>. The comparisons between the different conditions and between the two codes are all presented in this paper.

## II. Geometry Description

The geometries used for the current study were the results of the aforementioned effort by Lacy and Sclafani<sup>1</sup> to provide relevant commercial transport high-lift geometries for the public domain. These geometries used the original high-speed CRM as a starting point. After several iterations, the final high-lift CRM (HL-CRM) design has a wing that is similar to but not exactly the same as that of the high-speed CRM. Because the original CRM cruise geometry was designed for transonic speeds, a minor modification on the leading edge was needed to resolve high-lift issues at low speeds. Figure 1 illustrates the modification for the HL-CRM configuration, as the effective leading-edge radius was increased to resolve the high-lift issues. The HL-CRM also has leading-edge and trailing-edge devices that will provide the optimum position of the slats and flaps for landing and takeoff. The fuselage for the HL-CRM is essentially the same as the high-speed geometry. The high-speed CRM was configured with a flow-through fan cowl that was attached to the wing with a pylon. For the HL-CRM, the existing nacelle and pylon were used but were shortened to simplify the flaps-down modeling. For more information on the geometries used for this study, see reference 1.

The results presented in this paper were obtained on three different configurations – a cruise configuration, a landing configuration with inboard and outboard slats set at 30 degrees and inboard and outboard flaps set at 37 degrees, and a takeoff configuration with inboard and outboard slats set at 22 degrees and inboard and outboard flaps set at 25 degrees. All of these configurations had the nacelle/pylon assembly but no horizontal tail was included for this study.

## III. Grid Generation

The GridTool/VGRID software system<sup>4</sup>, part of the NASA Langley Tetrahedral Unstructured Software System (TetrUSS) CFD software suite, was used to generate unstructured grids for this study. VGRID uses an advancing-front method for Euler tetrahedral grids, and an advancing-layer method for thin-layer viscous grids required for Navier-Stokes analysis. In defining a computational domain, boundaries are represented by watertight bilinear surface patches that are constructed in GridTool based on user-specified geometries and an IGES Computer-aided Design (CAD) definition. Grid characteristics like cell spacing, smoothness, and anisotropic stretching are specified in GridTool by global parameters and the local placement of volume, nodal, and linear sources.

A surface mesh is generated in VGRID by triangulating each surface patch with a two-dimensional advancing-front method. Completed surface patch triangles then form the initial front for the generation of three-dimensional volume cells by the advancing-layer and advancing-front methods. Smooth variation of grid spacing is achieved with an exponential growth function, using GridTool-defined parameters and sources as inputs.

Twelve semispan grids were generated for this study. HL-CRM geometry configurations for cruise, landing, and takeoff were gridded for both flight and wind tunnel Reynolds numbers, and for use with the cell-based USM3D flow solver and the node-based FUN3D flow solver. Table 1 summarizes the grid sizes.

Table 1: Grid Size Summary  
*\* Denotes the degrees of freedom relevant to each flow solver*

Configuration	Condition	USM3D Grid		FUN3D Grid	
		Cells*	Nodes	Cells	Nodes*
Cruise	Flight	32,295,003	5,484,396	188,746,683	31,931,493
Cruise	Tunnel	32,303,982	5,485,050	187,695,535	31,751,576
Landing	Flight	79,629,043	13,498,605	478,521,805	80,846,771
Landing	Tunnel	95,162,152	16,134,442	544,895,268	92,079,063
Takeoff	Flight	92,644,673	15,705,965	548,333,761	92,644,541
Takeoff	Tunnel	90,906,833	15,413,005	534,035,588	90,234,771

USM3D used a pure tetrahedral grid (VGRID default), while FUN3D made use of a preprocessor to convert each base tetrahedral grid into a mixed-element grid. This mixed element grid was still composed of tetrahedra in the inviscid region, but viscous layer elements were converted into triangular prisms. Pyramid shaped elements were added to patch the outer boundary of prismatic layers with the interior boundary of tetrahedra to avoid creation of hanging nodes in the grid. Viscous layer spacing and distribution were controlled for each grid and flow solver using global parameters in GridTool. For USM3D grids, the viscous layer regions were resolved by approximately 40 layers, with a first layer height of  $y^+ = 1.0$  and first layer cell center heights ranging between  $y^+ = 0.25$  and  $y^+ = 0.75$  (this range is due to the way tetrahedra are stacked within each triangular prismatic layer created by VGRID). FUN3D viscous layer regions were resolved with approximately 60 layers and a first layer and first node height of  $y^+ = 0.5$ .

For each configuration and condition, the cell-based USM3D grid variation was generated first since it was a smaller grid and more amenable to fine-tuning and resolving gridding issues. VGRID's "ifact" scaling parameter was then used to globally scale the advancing-front method (both surface and volume) to refine the USM3D grid for use with FUN3D and provide a consistent number of degrees of freedom between the two flow solvers. An ifact value of 0.52 achieved a close match between the number of cells in the USM3D grids and the number of nodes in the FUN3D grids. All grids were generated on an Apple Mac Pro workstation with 3.5GHz Intel Xeon E5 "Ivy Bridge" processors. Grid generation wall clock times ranged from 1 to 2.5 hours for USM3D grids and 3 to 8 hours for FUN3D grids.

Surface meshes from the cruise, landing, and takeoff grids at flight Reynolds number are shown in Figures 2-7 (for easier visualization, only the coarser USM3D meshes are shown). Grid cross-sections from the flight Reynolds number landing configuration meshes for both USM3D and FUN3D are shown in Figures 8 and 9, respectively, at a spanwise plane of  $y=249''$  (approximately midspan along the inboard slat and flap). These cross sections show the relative difference in USM3D and FUN3D grids needed to achieve the same numerical resolution, and also illustrate the level of fidelity and smoothness designed into the grids to properly capture high-lift flows while maintaining practical grid sizes. This level of fidelity was based on prior experience and one iteration of manual grid refinement work, running solutions and studying various flow quantities to verify that the slat region was adequately resolved to handle transonic effects and to ensure that the main element wake flows were carried smoothly across the trailing-edge flap upper surface.

## IV. Flow Solvers and Computing Platform

### A. USM3D

The NASA Langley unstructured computational fluid dynamics code USM3D 6.0<sup>5-7</sup>, also part of TetrUSS, was used for Navier-Stokes analysis in this study. Within the tetrahedral cell-centered, finite volume flow solver, inviscid flux quantities are computed across each cell face using one of the following schemes: Roe's flux difference splitting (FDS)<sup>9</sup>, Advection Upstream Splitting Method (AUSM), Flux Vector Splitting (FVS), or Harten, Lax, and van Leer with Contact restoration (HLLC). A novel reconstruction process is used for spatial discretization, based on an analytical formulation for computing gradients within tetrahedral cells. Solutions are advanced to a steady state condition using an implicit backward-Euler time-stepping scheme. For numerical stability, limiter options include MinMod and Superbee flux limiters and an Eigen-value limiter. Turbulence closure in USM3D 6.0 is given by the one equation Spalart-Allmaras (SA)<sup>10</sup> model, the two-equation  $k-\epsilon$  turbulence model, or the two-equation Menter SST model. For the present study, Roe's FDS and Spalart-Allmaras turbulence model were used. To improve the prediction of skin friction drag, a solution limiter was not activated.

Solutions presented in this paper were obtained by running USM3D on the Pleiades supercomputer at the NASA Advanced Supercomputing (NAS) facility at NASA Ames Research Center. USM3D runs used 1024 cores and typically required 5 hours of wall clock time to run to convergence over 40,000 iterations, with global CFL number ramped from 5 to 250 over the first 200 iterations. Convergence was judged by tracking the solution residual and integrated aerodynamic performance coefficients until they settled out in a satisfactory fashion. Forces and moments were computed by evaluating pressure and skin friction forces on the CRM surface.

## B. FUN3D

FUN3D is an unstructured-grid flow solver developed originally by Anderson and Bonhaus<sup>8</sup>. This code has gone through significant modifications over the years by a team of researchers at NASA Langley using modern software practices.<sup>11</sup> The discrete form of the governing equations are solved either in a time-accurate manner with a constant time step at every grid point or with variable time stepping to accelerate convergence to a steady state. At each iteration step, a linear system of equations is relaxed with a point implicit procedure<sup>12</sup>. FUN3D can accommodate multiple types of grid elements including tetrahedrons, prisms, pyramids and hexahedrons, which makes it compatible with many different grid generators. For the current work, Roe's flux-difference splitting scheme<sup>9</sup> is used without a flux limiter. Although several turbulence models are available in FUN3D, ranging from the one-equation Spalart-Allmaras (SA)<sup>10</sup> model to a full Reynolds Stress model, the current solutions were obtained using the SA model for consistency with USM3D solutions.

The present solutions were obtained on the NASA Advanced Supercomputing (NAS) facility at the NASA Ames Research Center using 2800 cores, as well as on the NASA Langley Research Center midrange K-cluster using 480 cores. The FUN3D code was run in a steady mode for the majority of the cases, until the forces converged to within 1% of the final values. Such solutions required anywhere from 20,000 iterations to 80,000 iterations, although most cases converged within 40,000 iterations, requiring approximately 10 hours on 2800 cores on the NAS computer system.

## C. Boundary and Flow Conditions

Outer boundaries of the computational domain were treated as characteristic inflow/outflow surfaces with freestream conditions specified by Reynolds number, Mach number, flow angle, and static temperature. These conditions are summarized in Table 2 below (note that flight conditions correspond to 10,000 ft. altitude). Solutions were run over an angle-of-attack range from 0° to 20°. A reflection boundary condition was used at the symmetry plane of the semispan geometry. All aircraft surfaces were treated as no-slip viscous boundaries.

Table 2: Flow Conditions

Configuration	Condition	Reynolds Number	Mach Number	Static Temperature
Cruise	Flight	$24.60 \times 10^6$	0.2	483°R
Cruise	Tunnel	$3.27 \times 10^6$	0.2	519°R
Landing	Flight	$24.60 \times 10^6$	0.2	483°R
Landing	Tunnel	$3.27 \times 10^6$	0.2	519°R
Takeoff	Flight	$31.98 \times 10^6$	0.26	483°R
Takeoff	Tunnel	$4.24 \times 10^6$	0.26	519°R

## V. Results

### A. Cruise Configuration

This study started by looking at results for the cruise configuration. Cases were run with both codes at flight and wind tunnel test conditions. The flight conditions used were a Reynolds number of 24.6 million and a Mach number of 0.2. The wind tunnel conditions used were a Reynolds number of 3.27 million and a Mach number of 0.2. The angle-of-attack range was from 0° to 20° for both conditions for USM3D and from 0° to 12° for both conditions for FUN3D.

Figures 10 - 12 show comparisons of the lift curve, drag curve and drag polar, respectively, for the cruise configuration for both codes. The two codes predict the lift very closely up to ~10°, which is the extent of the linear



range of the lift curve, for both the flight and wind tunnel conditions. The drag also agrees well between the two codes up to  $\sim 10^\circ$  angle of attack for both conditions and the drag polar curves compare well up to stall.

Next, the surface pressures are presented in figures 13 - 15. To limit the size of this paper, we only present surface pressure results at three representative angles of attack for all three configurations. For the cruise configuration, the three angles of attack presented are  $4^\circ$ ,  $8^\circ$  and  $12^\circ$ . In each figure, the flight and wind tunnel conditions for USM3D are presented on top and then the flight and wind tunnel conditions for FUN3D are presented at the bottom. In each of the separate figures, the upper surface pressure distributions are shown at the top of the plot and the lower surface is presented below the upper surface.

Figure 13 shows that at  $4^\circ$  angle of attack, the lower surface pressure distributions look the same at both flight and wind tunnel conditions for both codes. For the upper surface pressures, though, USM3D predicts a wider area of low pressure (i.e., leading-edge suction) downstream of the leading edge than FUN3D. As shown in figure 14, at  $8^\circ$  angle of attack, both the upper and lower surface pressure distributions agree well at both flight and wind tunnel conditions for both codes. At  $12^\circ$  angle of attack, the USM3D flight and wind tunnel upper surface pressures differ between each other beginning just aft of the nacelle all the way to the wing tip while the lower surface pressures agree fairly well, as seen in figure 15. This figure also shows noticeable differences between the FUN3D flight and wind tunnel upper surface pressures but the lower surface pressures compare well. As expected, both codes accurately predict the lower surface pressures because our methods are very reliable in a compressed flow field. The differences occur on the upper surface in the expansion flow field. Therefore, differences between FUN3D and USM3D were expected due to the node-based and cell-centered approaches as well as differences in grid topology. These manifest on the inboard upper surface and aft of the nacelles for both flight and wind tunnel conditions.

## B. Landing Configuration

Next, the results for the landing configuration are examined. Cases were run with both codes at flight and wind tunnel test conditions. As for the cruise configuration, flight conditions used were at a Reynolds number of 24.6 million and a Mach number of 0.2. The wind tunnel test conditions were run at a Reynolds number of 3.27 million and a Mach number of 0.2. The angle-of-attack range was from  $0^\circ$  to  $20^\circ$  for flight and  $0^\circ$  to  $17^\circ$  for the wind tunnel conditions with FUN3D and  $0^\circ$  to  $18^\circ$  for the wind tunnel conditions with USM3D.

Figure 16 shows the comparison of the lift curves for the landing configuration for both codes. For the flight Reynolds number condition, FUN3D predicts a lower lift than USM3D from  $0^\circ$  to  $6^\circ$  and from  $15^\circ$  to  $20^\circ$  angle of attack and indicates a break in the lift at  $19^\circ$  angle of attack while USM3D does not predict this break. The two codes compare well from  $8^\circ$  to  $14^\circ$  angle of attack for the flight Reynolds number condition. FUN3D also predicts a lower lift for the wind tunnel Reynolds number condition from  $0^\circ$  to  $8^\circ$  angle of attack while comparing well from  $10^\circ$  to  $14^\circ$ . At  $15^\circ$  angle of attack, FUN3D begins to show wing stall while USM3D does not indicate a stall beginning until  $17^\circ$  angle of attack. The drag comparison is shown in figure 17. This figure indicates that USM3D predicts slightly higher drag values than FUN3D for both the flight and wind tunnel Reynolds number conditions except at  $17^\circ$  and  $20^\circ$  angle of attack. The drag polar for the landing configuration is presented in figure 18. This polar shows that the differences seen in the lift curves and drag curves were dependent on angle of attack since the drag polars compare well for both the flight and wind tunnel conditions up to where the wing stalls.

Next, the surface pressures are presented in figures 19 - 21. As for the cruise configuration, only three representative angles of attack are presented ( $4^\circ$ ,  $8^\circ$  and  $12^\circ$ ). Figure 19 shows that at  $4^\circ$  angle of attack, the upper surface and lower surface pressures between the two codes for both the flight and wind tunnel conditions compare reasonably well. At  $8^\circ$  angle of attack, as seen in figure 20, the surface pressures compare well for both codes for both conditions on the upper surface. Similar to the  $4^\circ$  cases, the lower surface pressures compare well between the two codes at both Reynolds number conditions. At  $12^\circ$  angle of attack, the flight pressure contours compare well for the codes themselves but differ between the two codes (figure 21). The upper surface flight pressure contour distributions for FUN3D show a larger area of low pressure just aft of the wing leading edge and a small area of high pressure at the outboard wing trailing edge that is not seen in the USM3D results. The wind tunnel Reynolds number condition results compare well between the two codes. The lower surface pressure distributions compare well between the two codes for both Reynolds number conditions.

## C. Takeoff Configuration

Finally, the takeoff configuration results are shown in figures 22 - 27. Cases were run with both codes at flight and wind tunnel test conditions. The flight conditions used were at a Reynolds number of 31.98 million and a Mach number of 0.26 while the wind tunnel test conditions used were at a Reynolds number of 4.24 million and a Mach number of 0.26. The angle-of-attack range was again from  $0^\circ$  to  $20^\circ$  for both sets of conditions for both codes.

Figures 22 - 24 show comparisons of the lift and drag curves and the drag polar, respectively, for the takeoff configuration for both codes. USM3D and FUN3D predict the lift curve to have the same slope but vary slightly in the magnitude of the lift coefficient over most of the angle-of-attack range, as seen in figure 22. Figure 23 indicates that once again USM3D predicts higher drag values than FUN3D for both the flight and wind tunnel Reynolds number conditions. Finally, the drag polar shown in figure 24 shows that, as seen for the landing configuration, the differences seen in the lift and drag curves were dependent on angle of attack since the drag polars compare well for both the flight and wind tunnel conditions up to where the lift begins to stall.

Next, the surface pressures are presented in figures 25 - 27. Once again only a representative subset of the angles of attack are presented ( $4^\circ$ ,  $8^\circ$  and  $16^\circ$ ). Figure 25 shows that at  $4^\circ$  angle of attack, the surface pressures look very similar at both flight and wind tunnel conditions for both codes on the upper and lower surfaces. The surface pressures also look very similar at  $8^\circ$  angle of attack (figure 26) at both flight and wind tunnel conditions for both codes on the upper and lower surfaces. Finally, figure 27 shows that the same comparison is true at  $16^\circ$  angle of attack, the surface pressures compare well at both flight and wind tunnel conditions for both codes on the upper and lower surface.

## VI. Conclusion

A computational assessment has been conducted to investigate baseline HL-CRM that cover both flight and wind tunnel Reynolds numbers. This study was performed with two unstructured CFD codes, USM3D and FUN3D. The results show that for the cruise configuration, the lift, drag and drag polar all compared well up to  $\sim 10^\circ$  angle of attack for both the wind tunnel and flight conditions. For the landing and takeoff configurations, the lift and drag did not compare as well between the codes at both flight and wind tunnel conditions but the drag polars did compare well, which indicates that the lack of agreement is dependent on angle of attack. This lack of agreement may be caused by the difference in how the two CFD codes handle the discretization of the viscous terms. This lack of agreement could also be caused by a difference in how the two CFD codes handle differences in the farfield boundary condition or possibly how the dissipation levels are handled in the two codes.

Surface pressure contours were also shown for both codes at both conditions (flight and wind tunnel) and on all three configurations. For the cruise configuration, the upper surface pressures at  $4^\circ$  and  $12^\circ$  angle of attack were different between the two codes for both the wind tunnel and flight condition. The lower surface pressure contours compared well over the angle-of-attack range except at  $12^\circ$  angle of attack where the surface pressures differ between the two codes for both the wind tunnel and flight conditions. The surface pressures for the landing configuration compare well on the upper and lower surface except at  $12^\circ$  angle of attack where the flight condition surface pressures differ between the two codes. Finally, the surface pressures for the takeoff configuration compare well on both the upper and lower surfaces.

## Acknowledgments

This study was supported by the Advanced Air Transport Technology (AATT) project at NASA.

## References

- <sup>1</sup> Lacy, D.S., and Sclafani, A.J., "Development of the High-Lift Common Research Model (HL-CRM): A Representative High Lift Configuration for Transonic Transports, AIAA Paper 2016-0308, January 2016.
- <sup>2</sup> Vassberg, J.C., DeHaan, M.A., Rivers, S.M., Wahls, R.A., "Development of a Common Research Model for Applied CFD validation," AIAA Paper 2008-6919, August 2008.
- <sup>3</sup> NASA Common Research Model, URL: <http://commonresearchmodel.larc.nasa.gov>, February 2008.
- <sup>4</sup> Pandya, M., Abdol-Hamid, K., Campbell, R., and Frink, N. "Implementation of Flow Tripping Capability in the USM3D Unstructured Flow Solver". AIAA-2006-919, January 2006.
- <sup>5</sup> Pandya, M., Frink, N., and Noack, R. "Progress Toward Overset-Grid Moving Body Capability for USM3D Unstructured Flow Solver". AIAA-2005-5118, June 2005.
- <sup>6</sup> Pandya, M., Frink, N., Abdol-Hamid, K., and Chung, J. "Recent Enhancements to USM3D Unstructured Flow Solver for Unsteady Flows". AIAA-2004-5201, August 2004.
- <sup>7</sup> Pandya, M., Abdol-Hamid, K., and Frink, N. "Enhancement of USM3D Unstructured Flow Solver for High-speed High-Temperature Shear Flows". AIAA-2009-1329, January 2009.
- <sup>8</sup> Anderson, W. and Bonhaus, D., "An Implicit Upwind Algorithm for Computing Turbulent Flows on Unstructured Grids," Computers and Fluids, Vol. 23, No. 1, 1994, pp. 1-22.

<sup>9</sup>Roe, P. L., 1981, "Approximate Riemann Solvers, Parameter Vectors, and Difference Schemes", *Journal of Computational Physics*, Vol. 43, pp. 357-372.

<sup>10</sup>Spalart, P. and Allmaras, S., "A One-Equation Turbulence Model for Aerodynamic Flows," AIAA Paper 92-0439, 1992.

<sup>11</sup>Alexandrov, N.; Atkins, H. L.; Bibb, K. L.; Biedron, R. T.; Gno o, P. A.; Hammond, D. P.; Jones, W. T.; Kleb, W. L.; Lee-Rausch, E. M.; Nielsen, E. J.; Park, M. A.; Raman, V. V.; Roberts, T. W.; Thomas, J. L.; Vatsa, V. N.; Viken, S. A.; White, J. A.; and Wood, W. A.: Team Software Development for Aerothermodynamic and Aerodynamic Analysis and Design. NASA TM-2003-212421, 2003.

<sup>12</sup>Nielsen, E. J., Lu, J., Park, M. A., and Darmofal, D. L., "An Implicit, Exact Dual Adjoint Solution Method for Turbulent Flows on Unstructured Grids," *Computers and Fluids*, Vol. 33, No. 9, 2004, pp. 1131-1155, See also AIAA Paper 2003-0272.

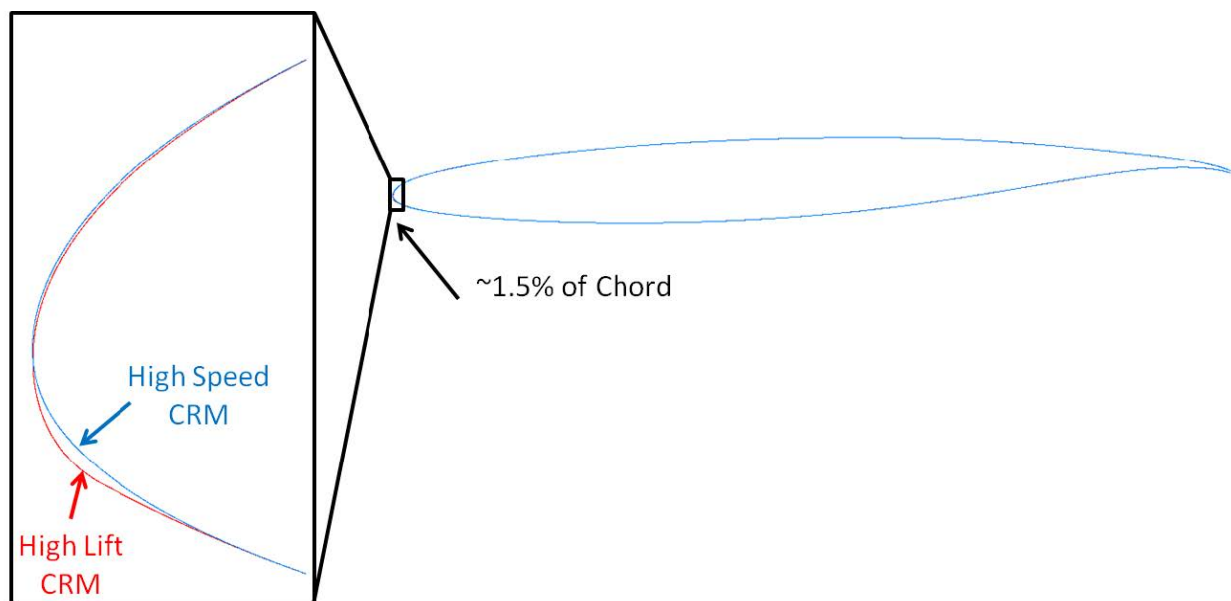


**Figure 1: Leading-edge modification of HL-CRM configuration (Lacy & Sclafani<sup>1</sup>).**

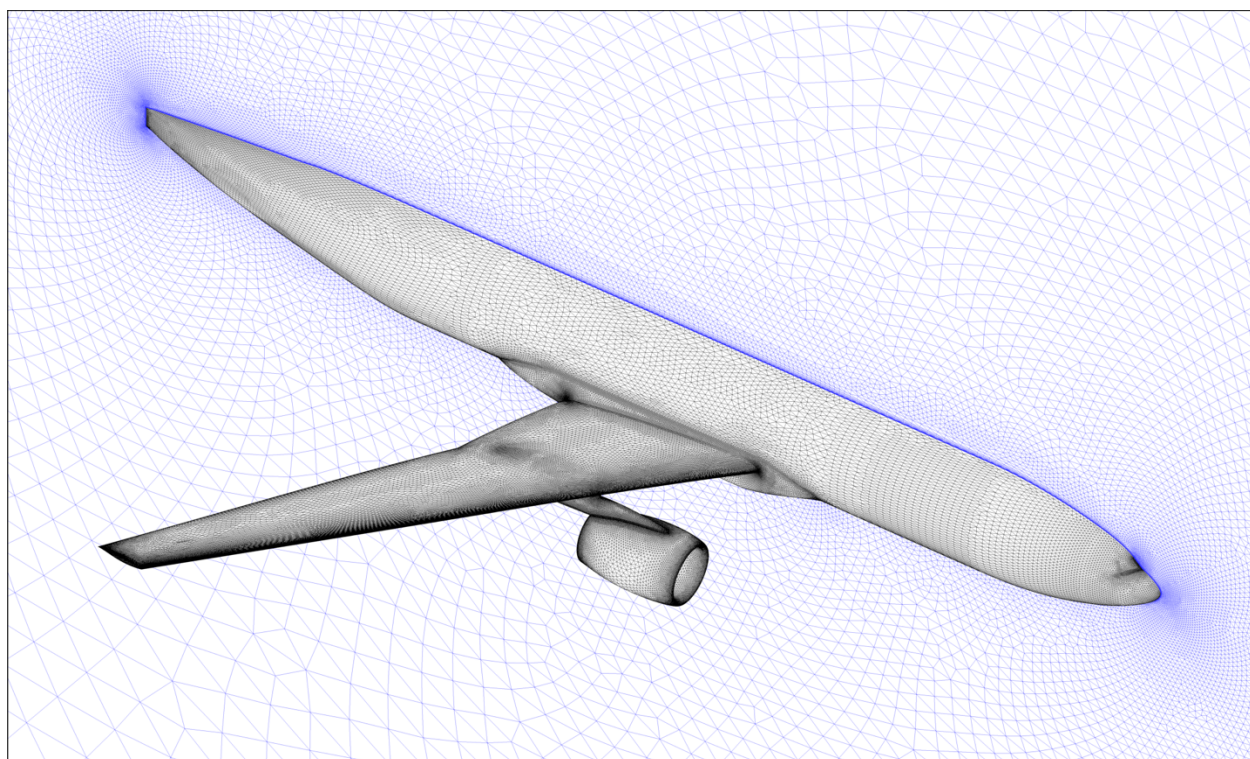


**Figure 2: USM3D Flight/Cruise Grid Mesh.**



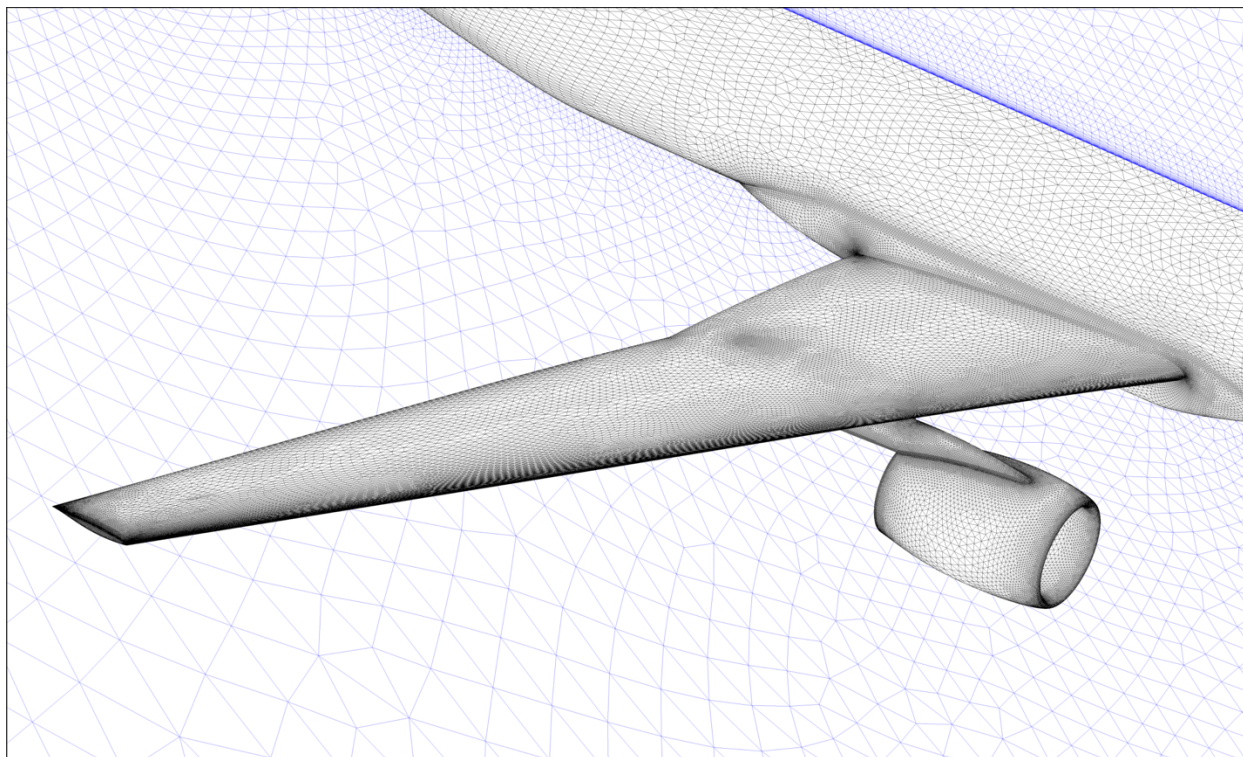


**Figure 3: USM3D Flight/Cruise Grid Mesh, Wing Close-up.**

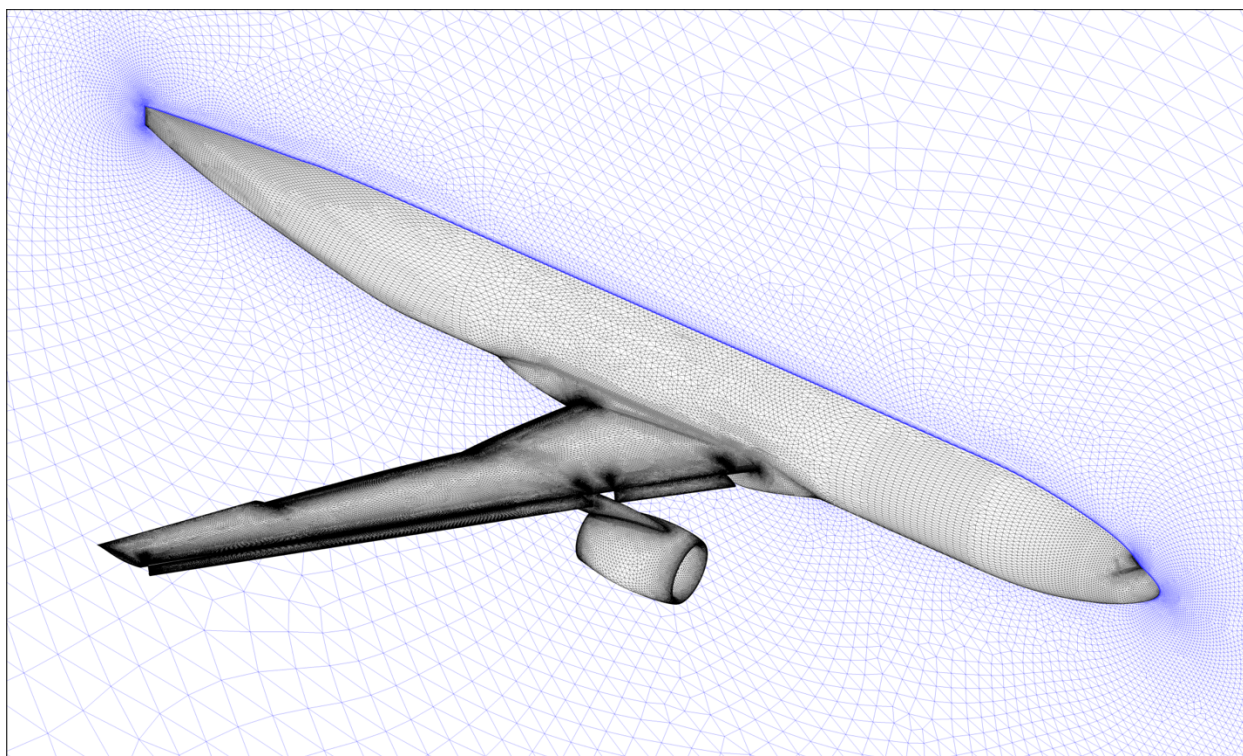


**Figure 4: USM3D Flight/Landing Grid Mesh.**



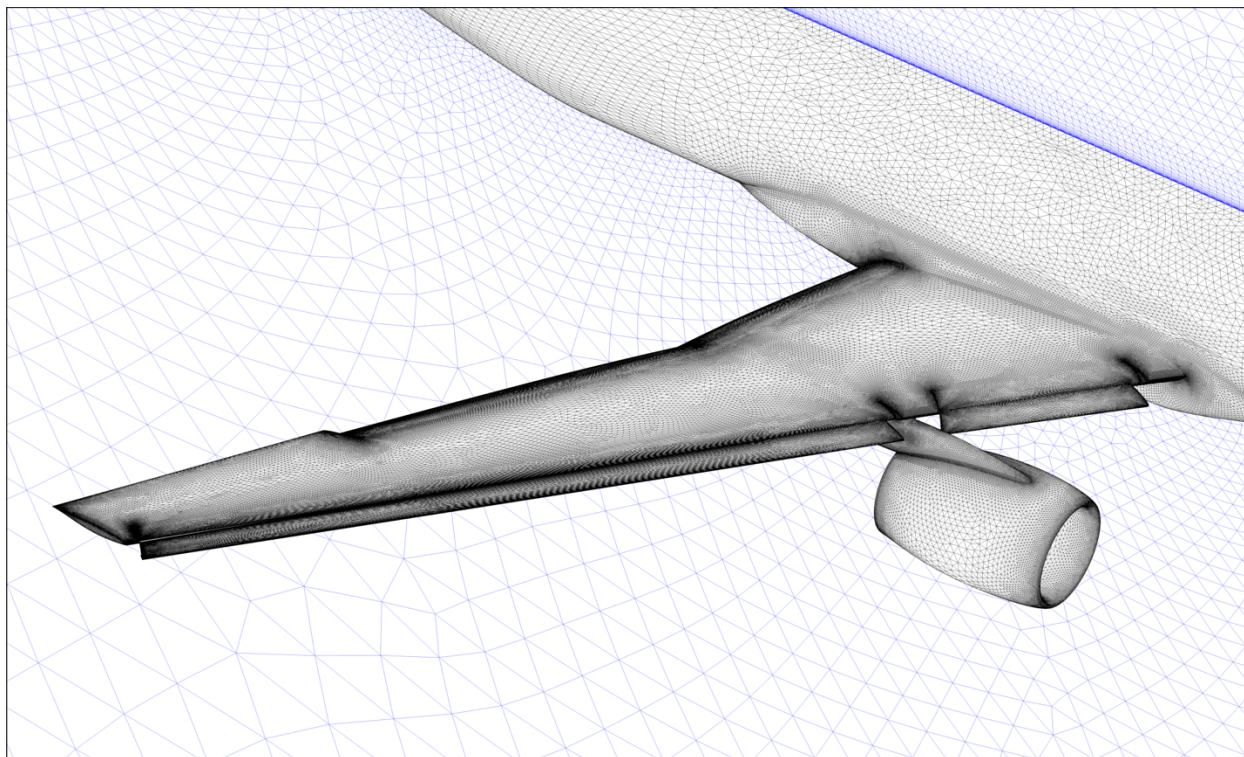


**Figure 5: USM3D Flight/Landing Grid Mesh, Wing Close-up.**

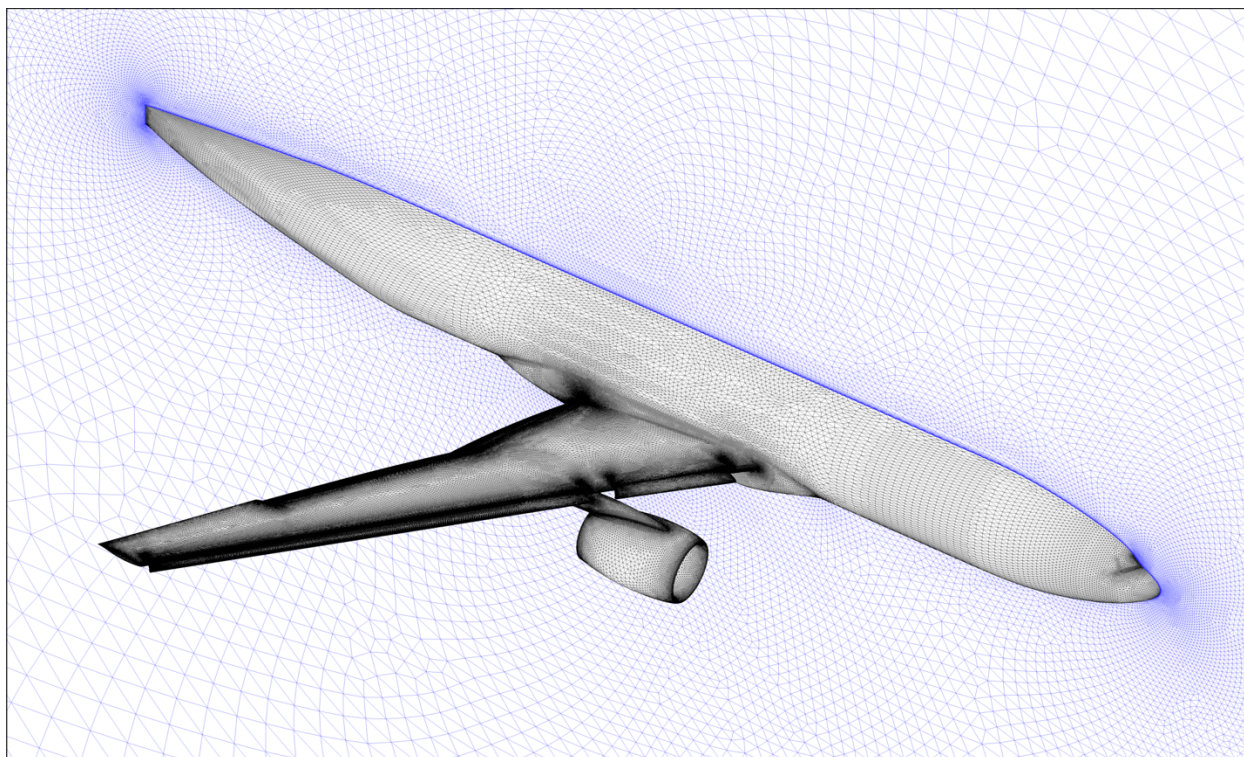


**Figure 6: USM3D Flight/Takeoff Grid Mesh.**



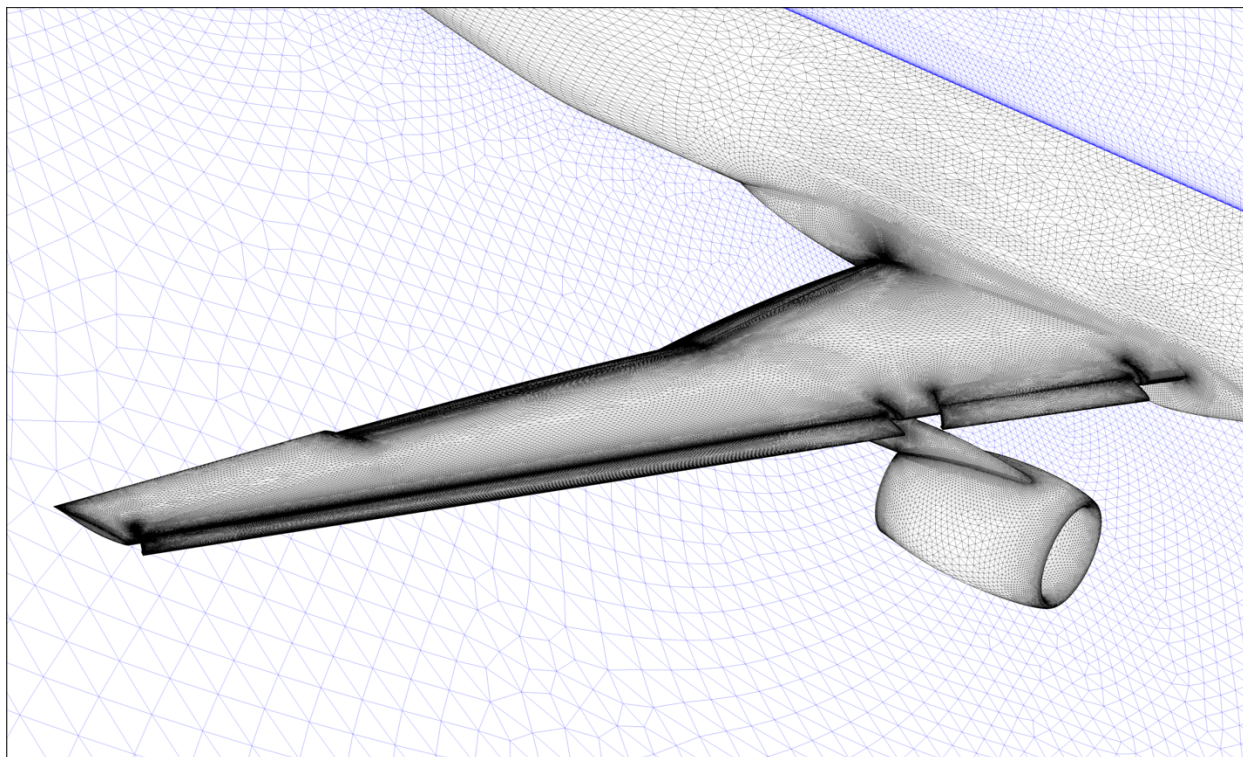


**Figure 7: USM3D Flight/Takeoff Grid Mesh, Wing Close-up.**

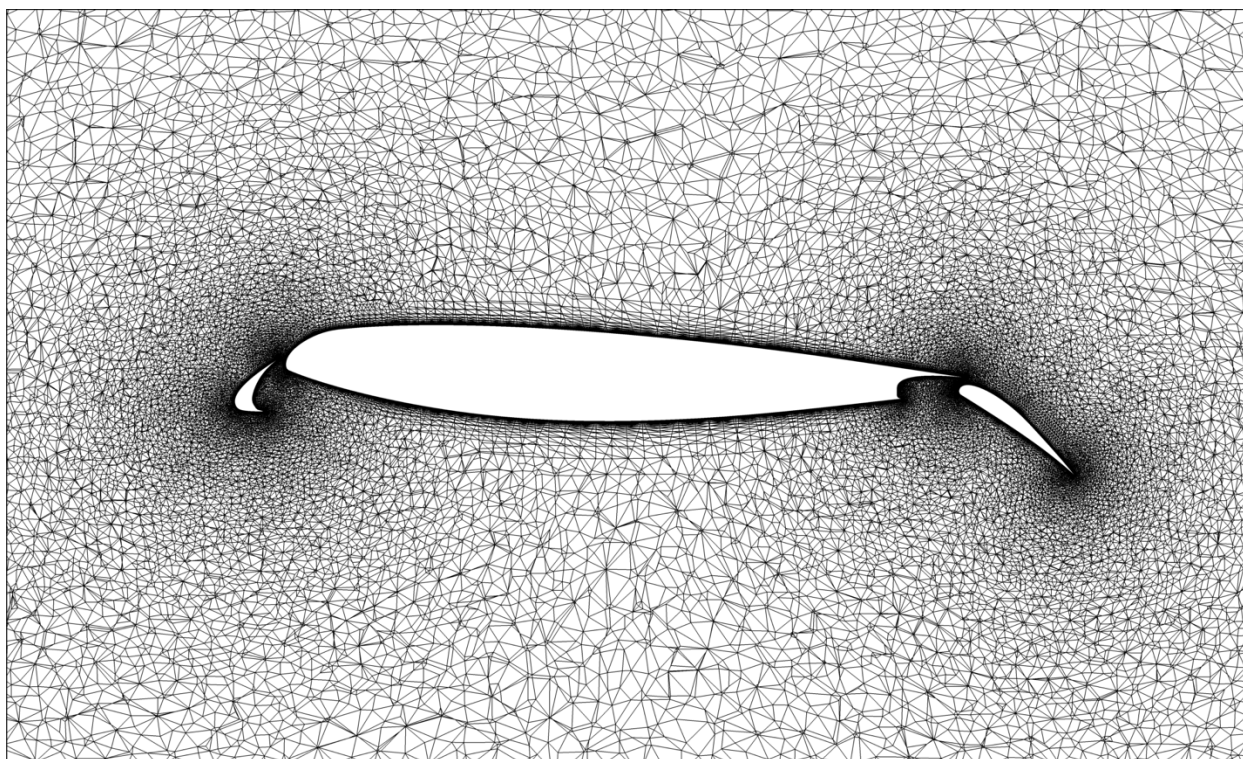


**Figure 8: USM3D Flight/Landing Grid Cross-section at  $y=249''$ .**

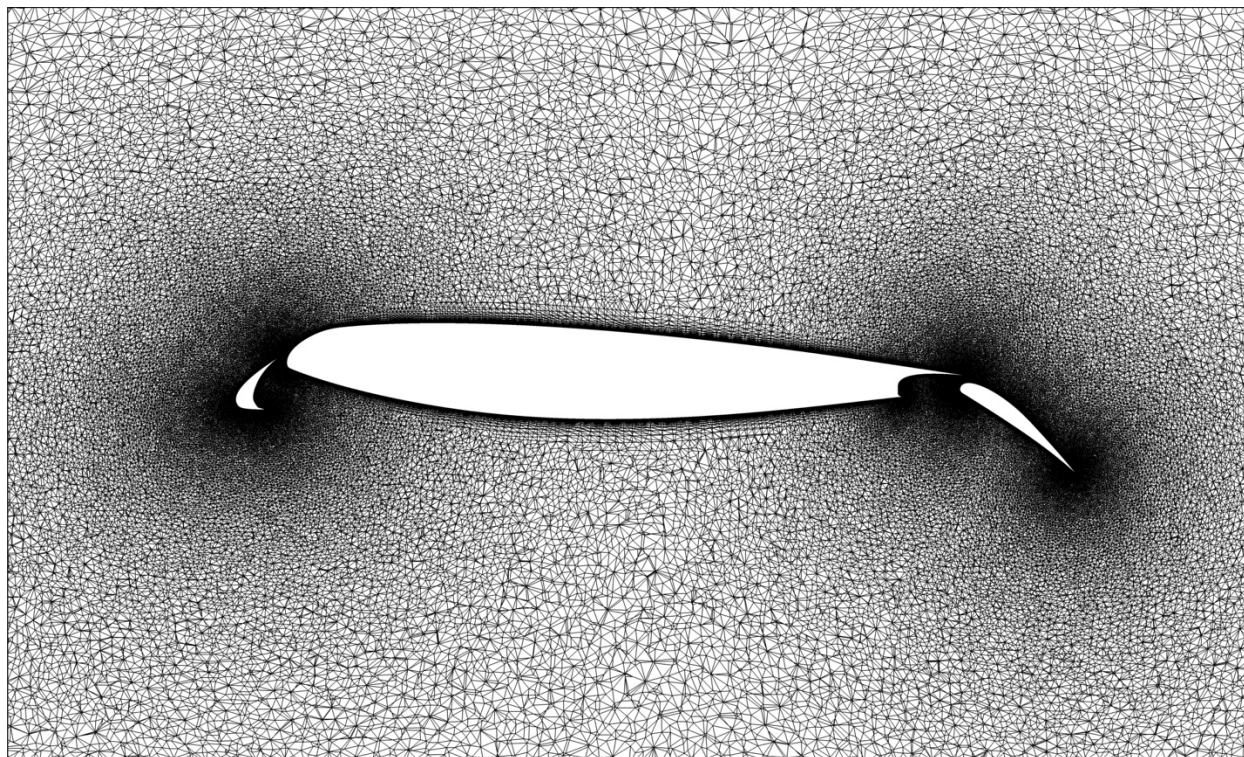


Figure 9: FUN3D Flight/Landing Grid Cross-section at  $y=249''$ .

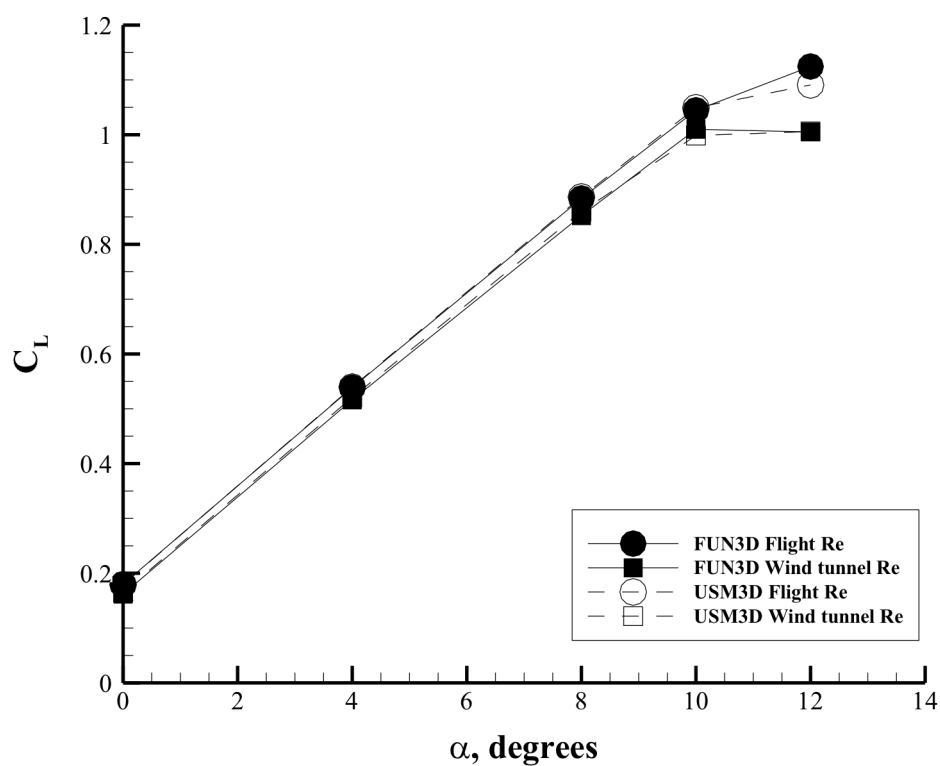


Figure 10. Cruise configuration lift curve,  $M=0.2$ ,  $Re=3.27$  million (wind tunnel) and 24.6 million (flight).

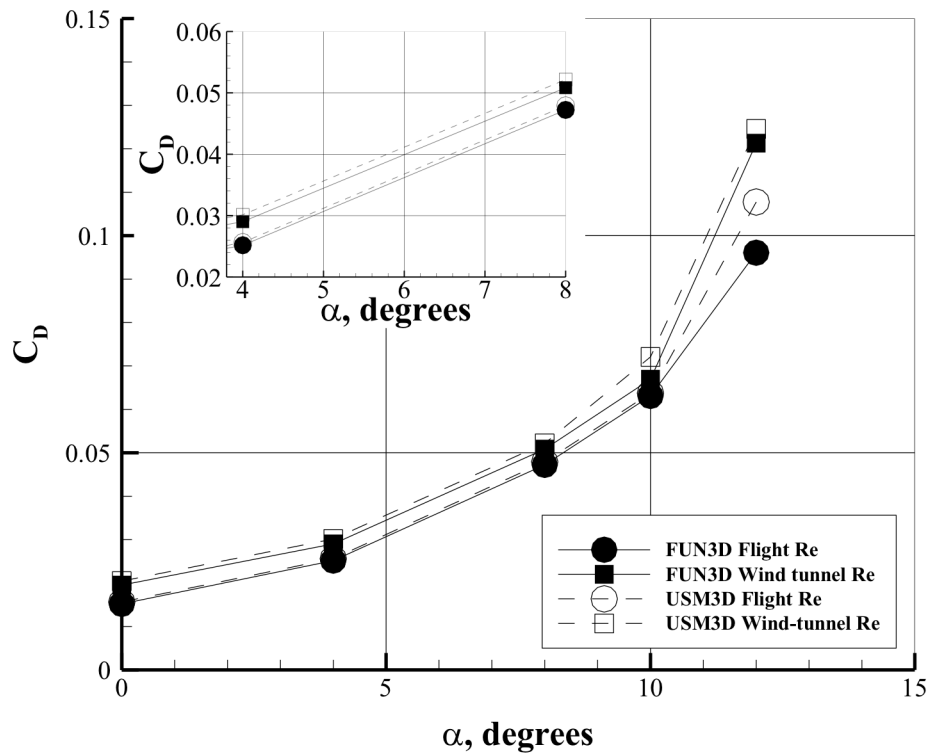


Figure 11. Cruise configuration drag curve,  $M=0.2$ ,  $Re=3.27$  million (wind tunnel) and  $24.6$  million (flight).

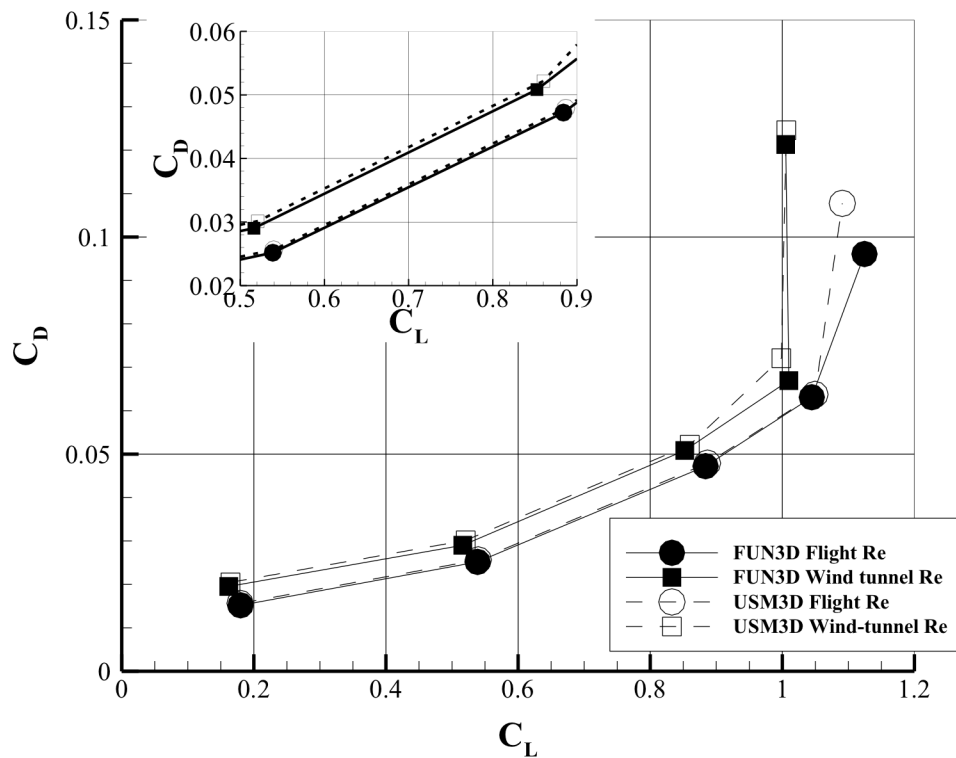
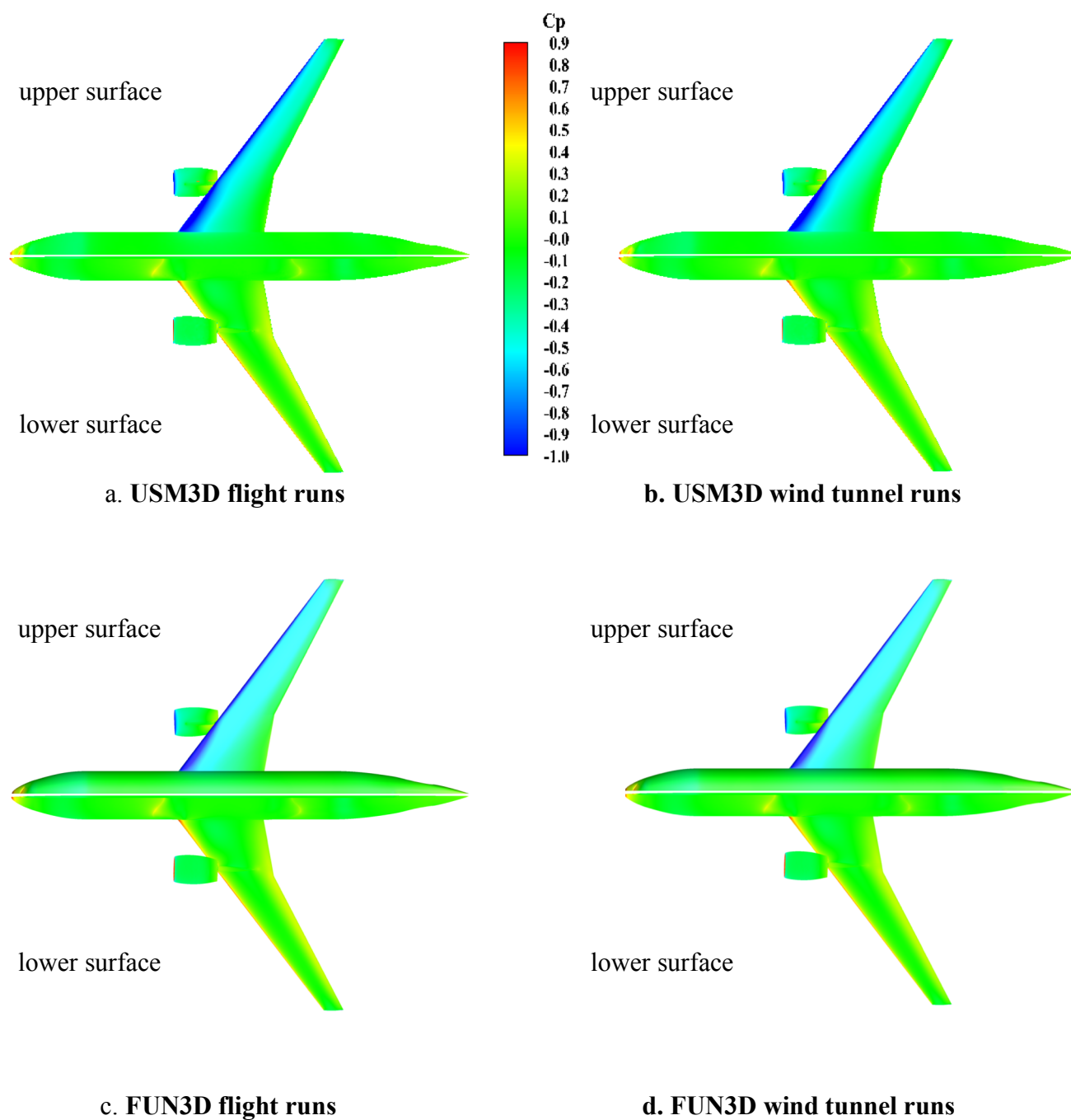


Figure 12. Cruise configuration drag polar,  $M=0.2$ ,  $Re=3.27$  million (wind tunnel) and  $24.6$  million (flight).





**Figure 13. Cruise configuration surface pressure contours,  $\alpha = 4^\circ$ ,  $M=0.2$ ,  $Re=3.27$  million (wind tunnel) and 24.6 million (flight).**



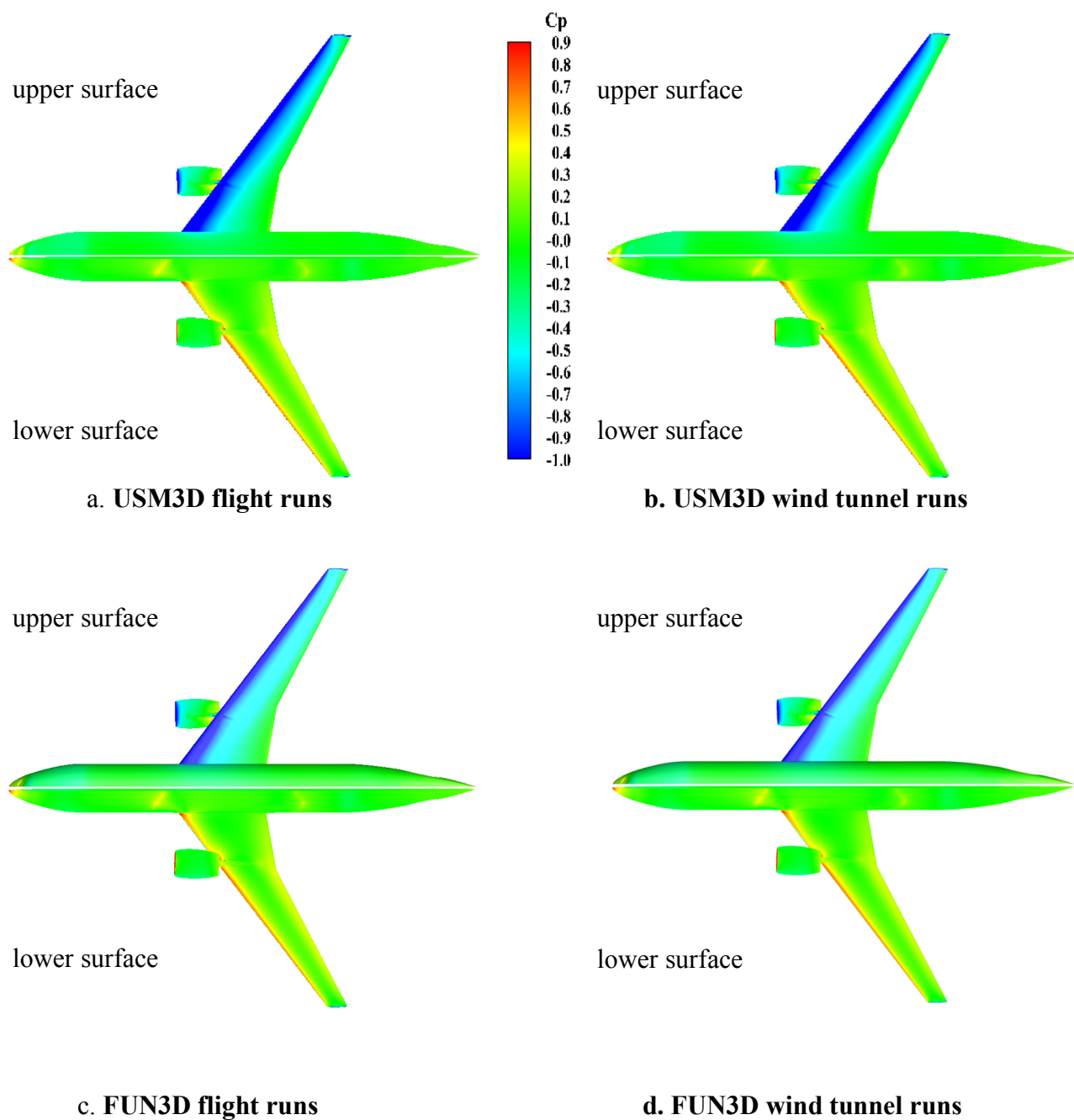


**Figure 14. Cruise configuration surface pressure distributions,  $\alpha = 8^\circ$ ,  $M=0.2$ ,  $Re=3.27$  million (wind tunnel) and  $24.6$  million (flight).**

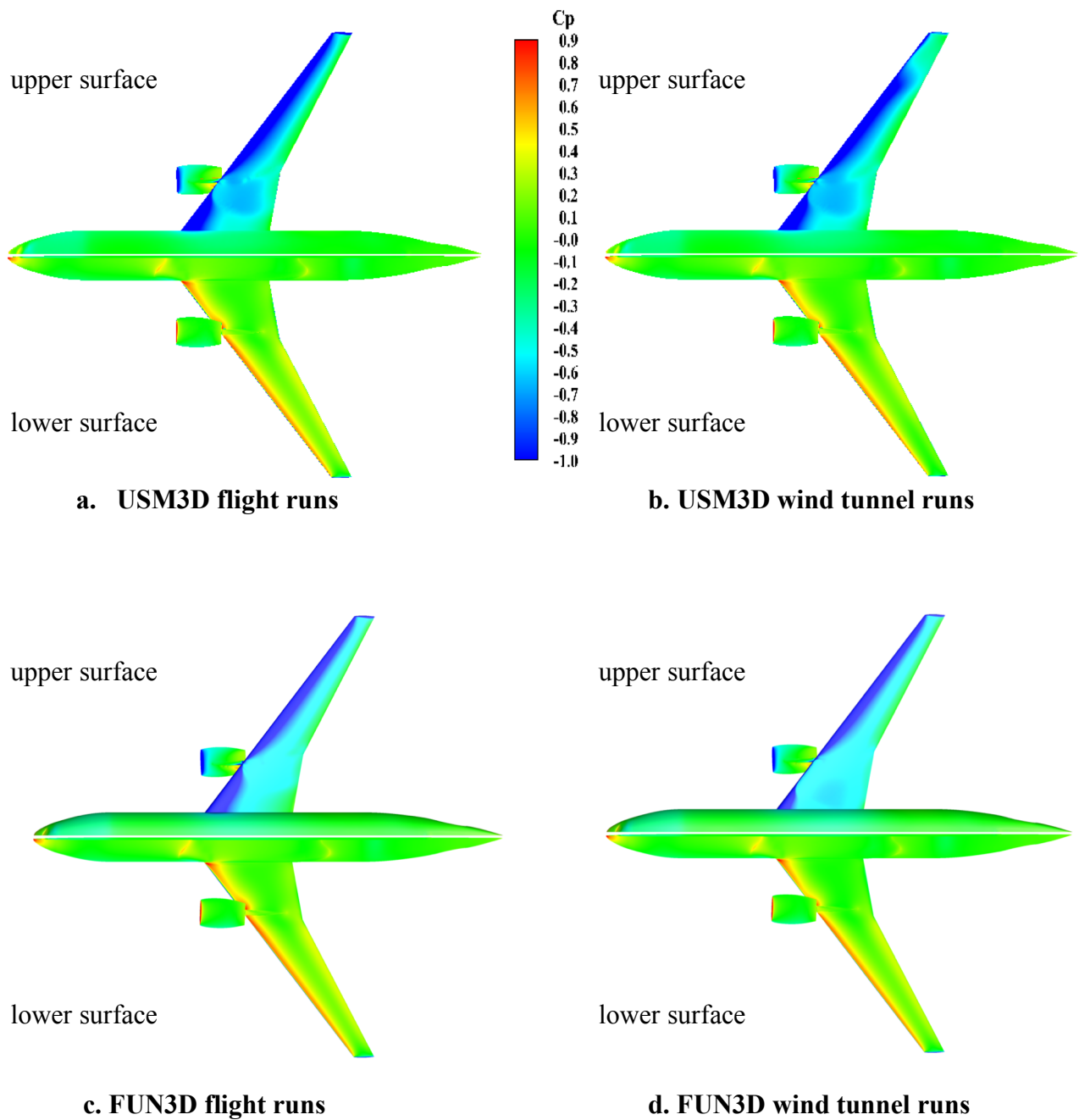


**Figure 15. Cruise configuration surface pressure distributions,  $\alpha = 12^\circ$ ,  $M=0.2$ ,  $Re=3.27$  million (wind tunnel) and  $24.6$  million (flight).**

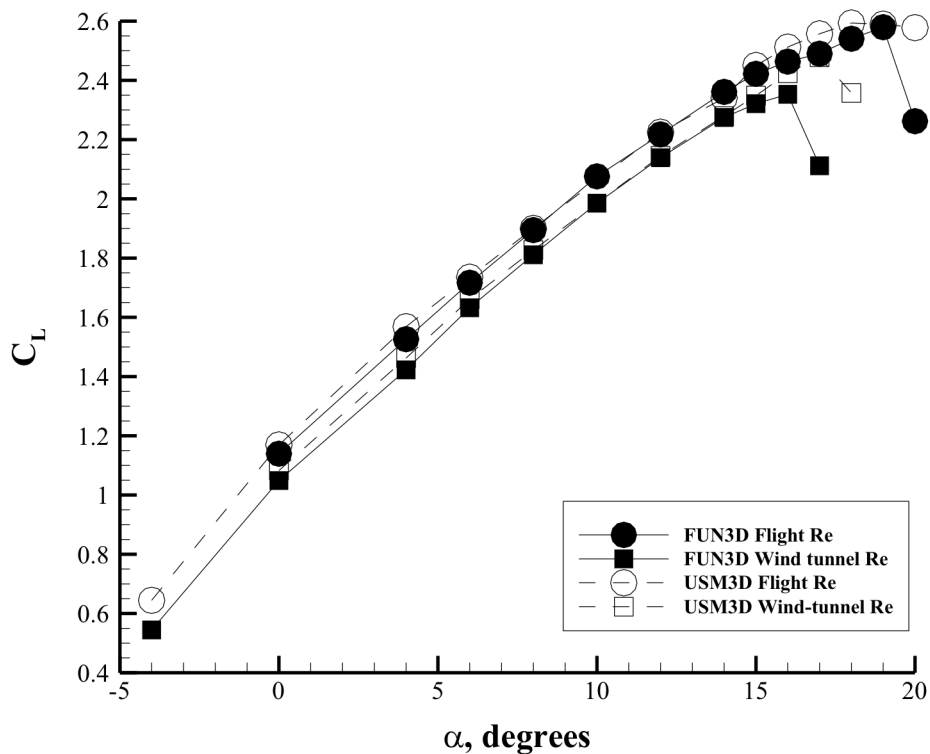


Figure 16. Landing configuration lift curve,  $M=0.2$ ,  $Re=3.27$  million (wind tunnel) and 24.6 million (flight).

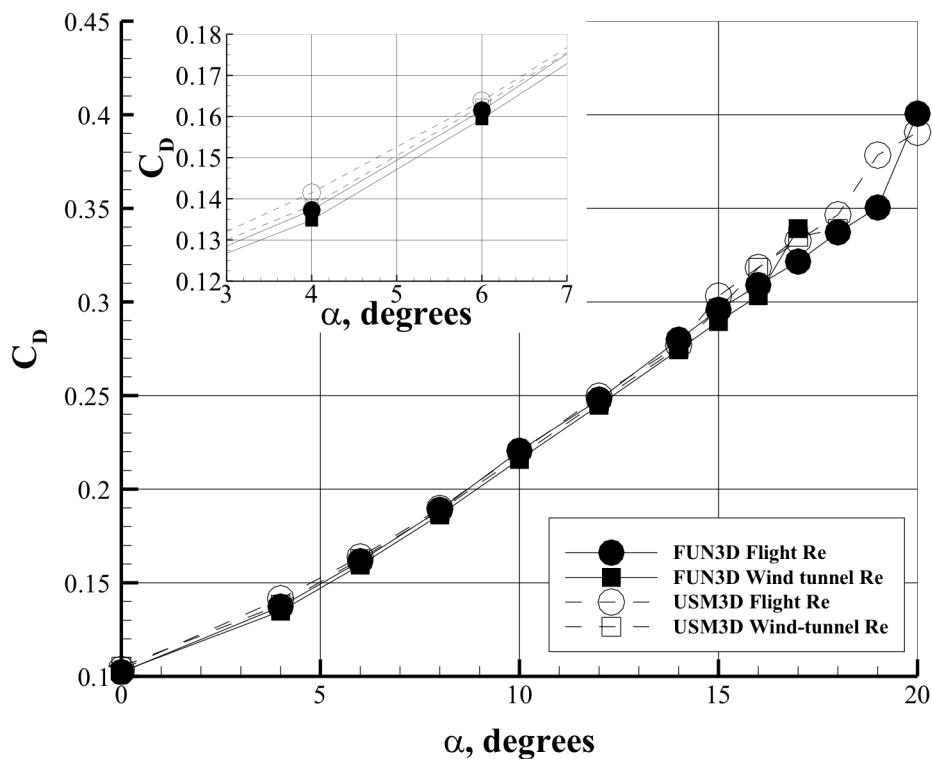
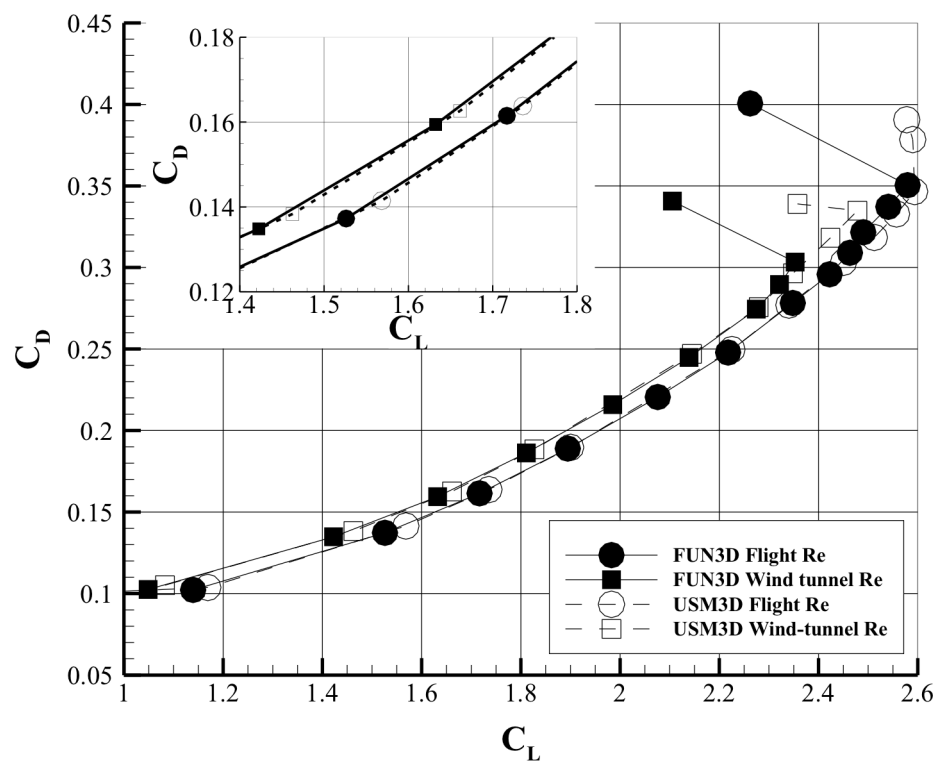
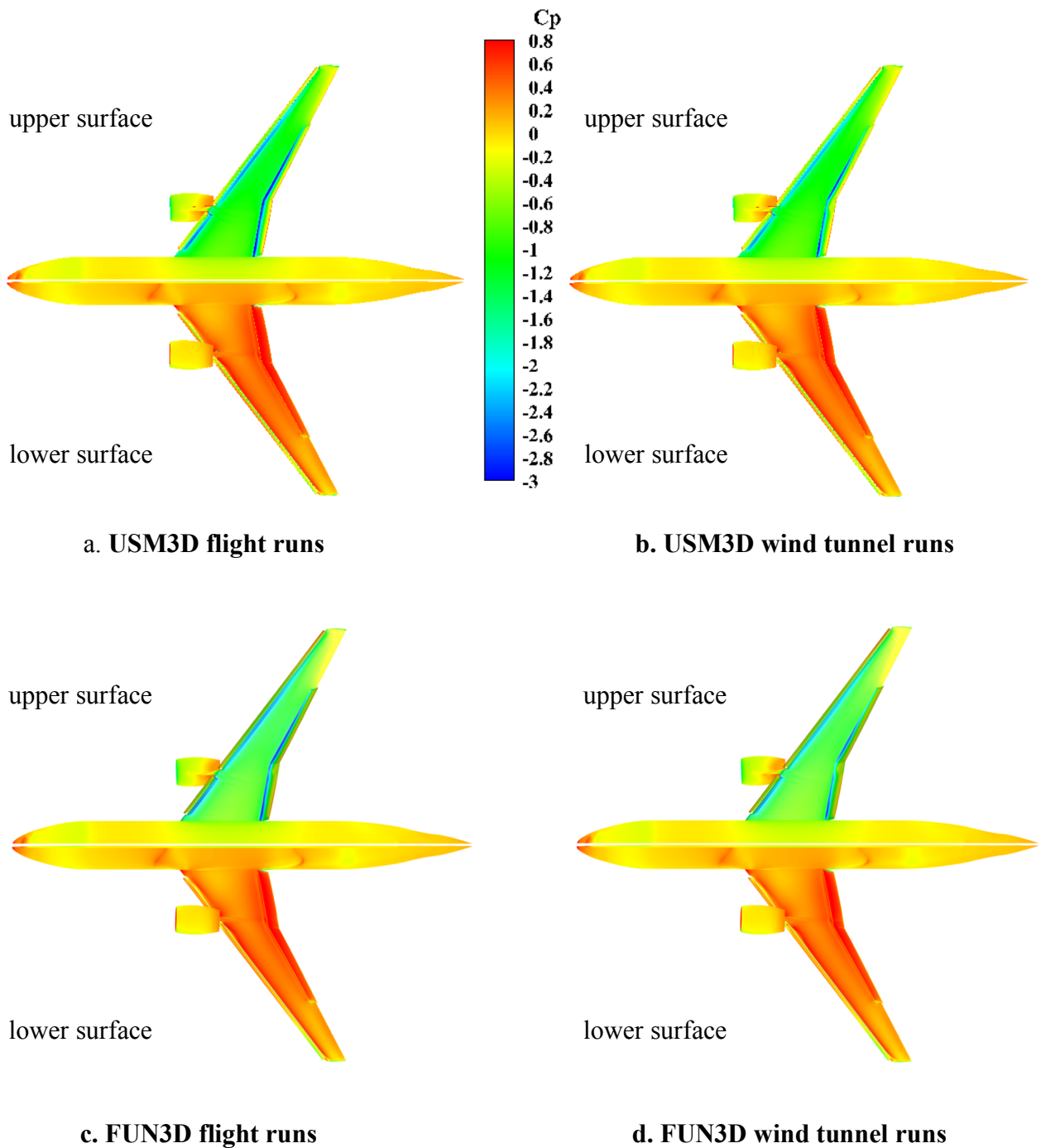


Figure 17. Landing configuration drag curve,  $M=0.2$ ,  $Re=3.27$  million (wind tunnel) and 24.6 million (flight).



**Figure 18. Landing configuration drag polar,  $M=0.2$ ,  $Re=3.27$  million (wind tunnel) and 24.6 million (flight).**



**Figure 19. Landing configuration surface pressure distributions,  $\alpha = 4^\circ$ ,  $M=0.2$ ,  $Re=3.27$  million (wind tunnel) and 24.6 million (flight).**



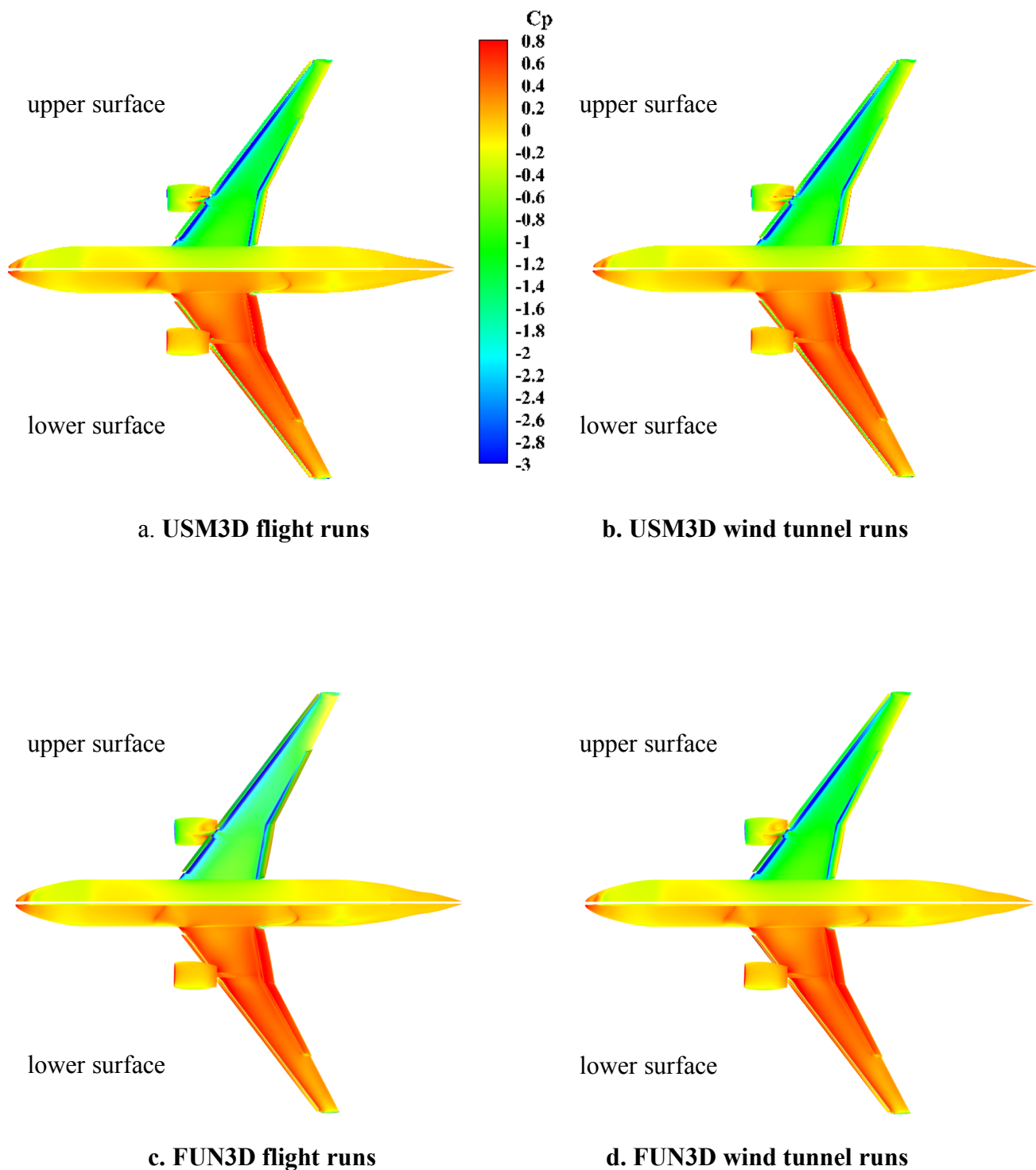


**Figure 20. Landing configuration surface pressure distributions,  $\alpha = 8^\circ$ ,  $M=0.2$ ,  $Re=3.27$  million (wind tunnel) and 24.6 million (flight).**

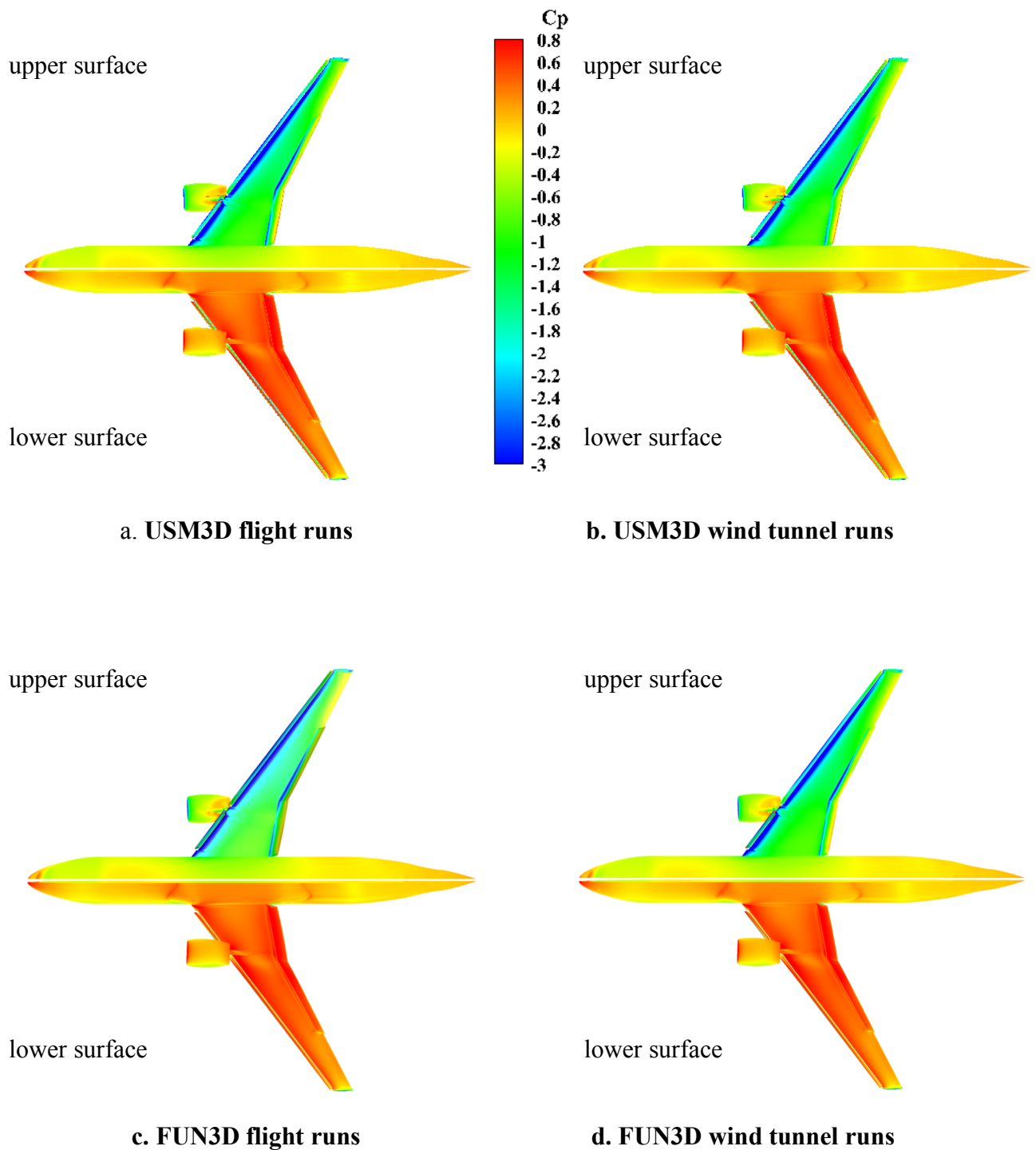


**Figure 21. Landing configuration surface pressure distributions,  $\alpha = 12^\circ$ ,  $M=0.2$ ,  $Re=3.27$  million (wind tunnel) and  $24.6$  million (flight).**

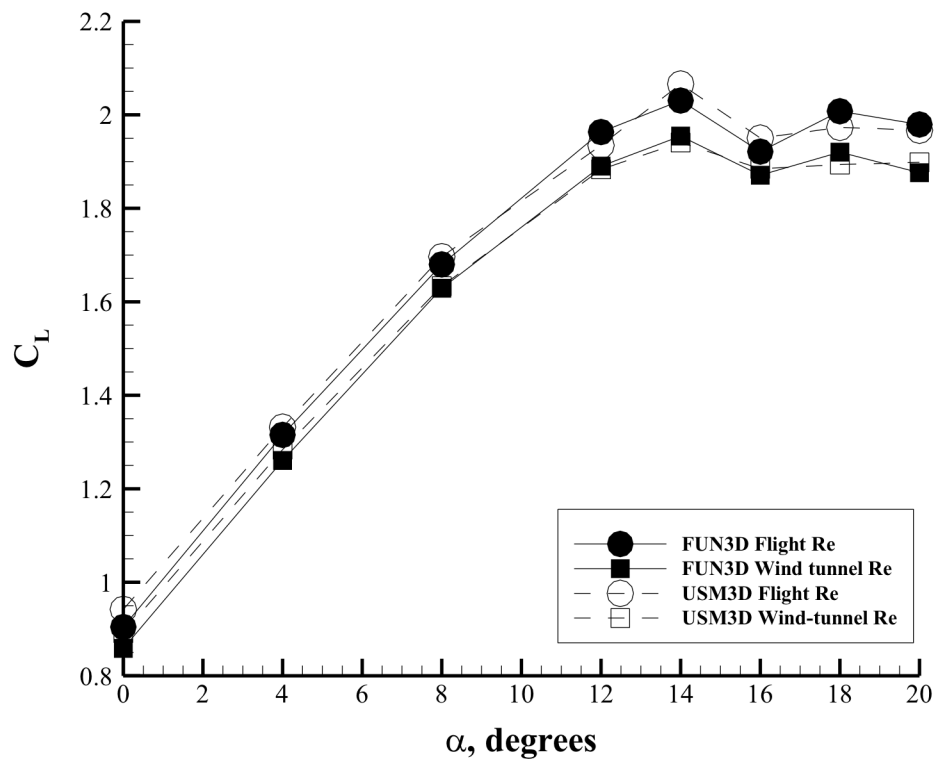


Figure 22. Takeoff configuration lift curve,  $M=0.26$ ,  $Re=4.24$  million (wind tunnel) and 31.98 million (flight).

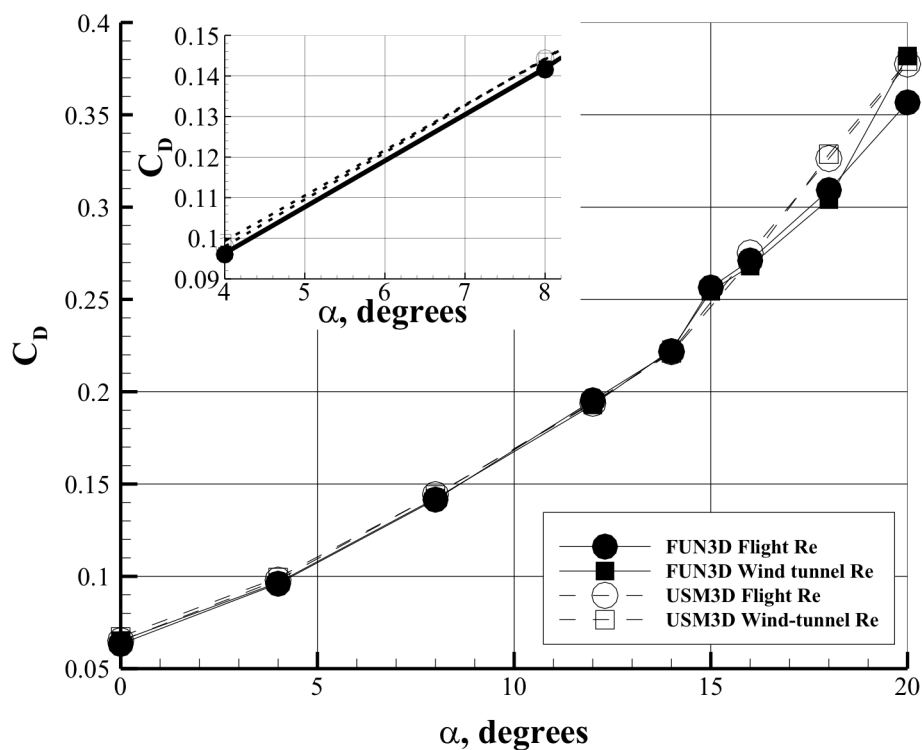
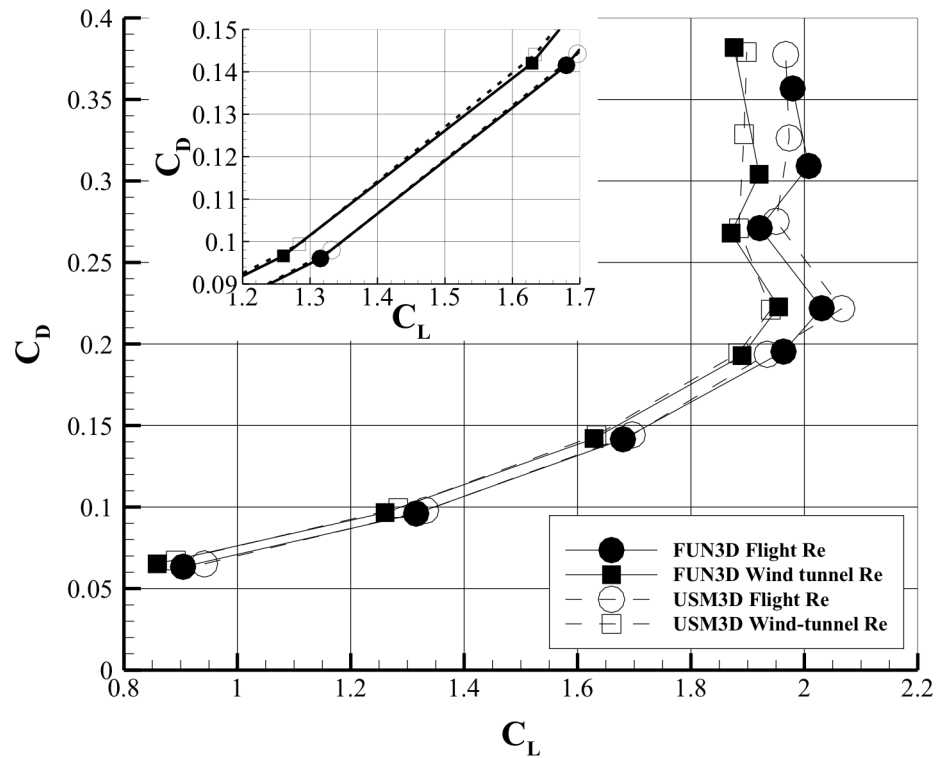
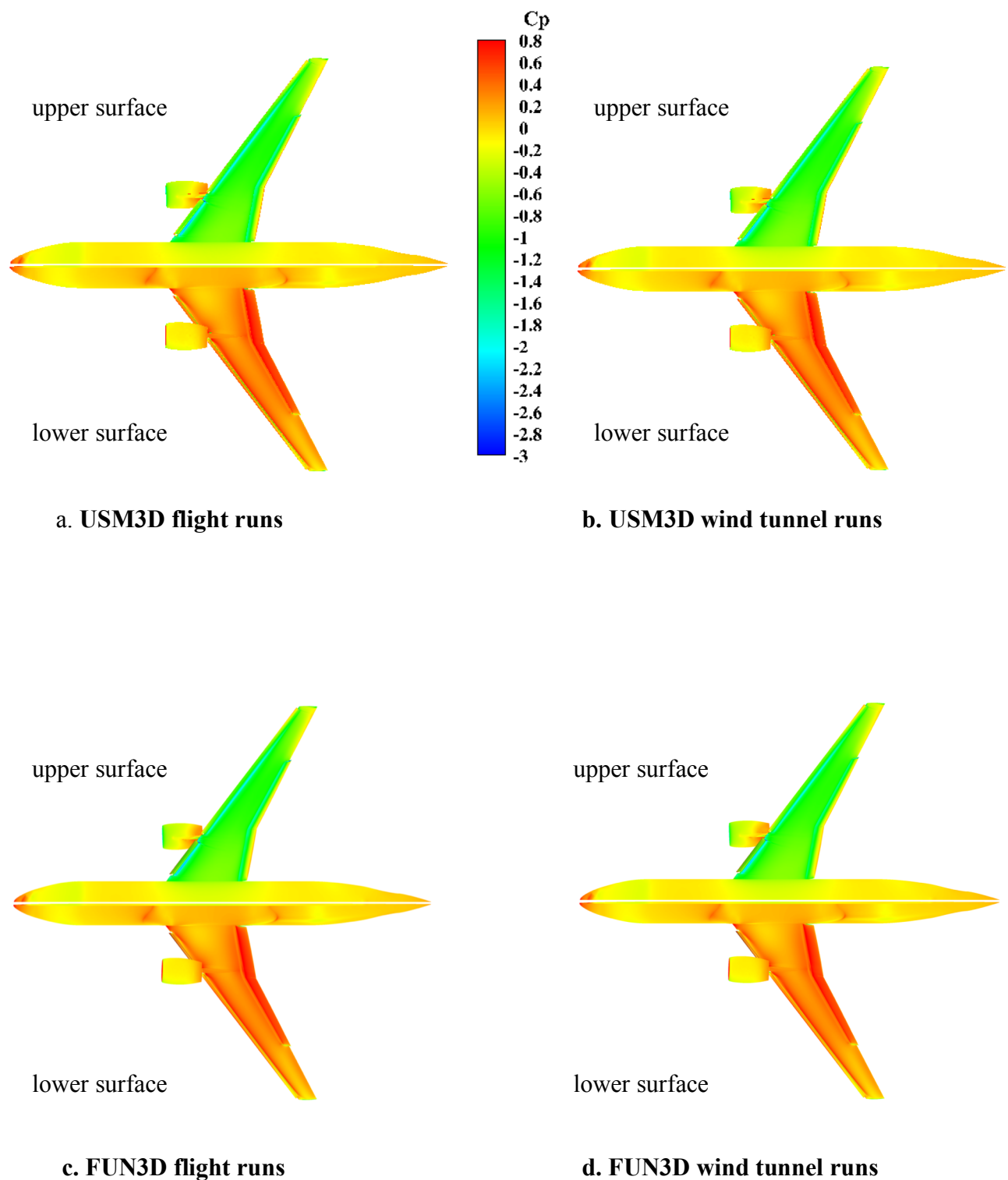


Figure 23. Takeoff configuration drag curve,  $M=0.26$ ,  $Re=4.24$  million (wind tunnel) and 31.98 million (flight).



**Figure 24. Takeoff configuration drag polar,  $M=0.26$ ,  $Re=4.24$  million (wind tunnel) and 31.98 million (flight).**



**Figure 25. Takeoff configuration surface pressure distributions,  $\alpha = 4^\circ$ ,  $M=0.26$ ,  $Re=4.24$  million (wind tunnel) and 31.98 million (flight).**



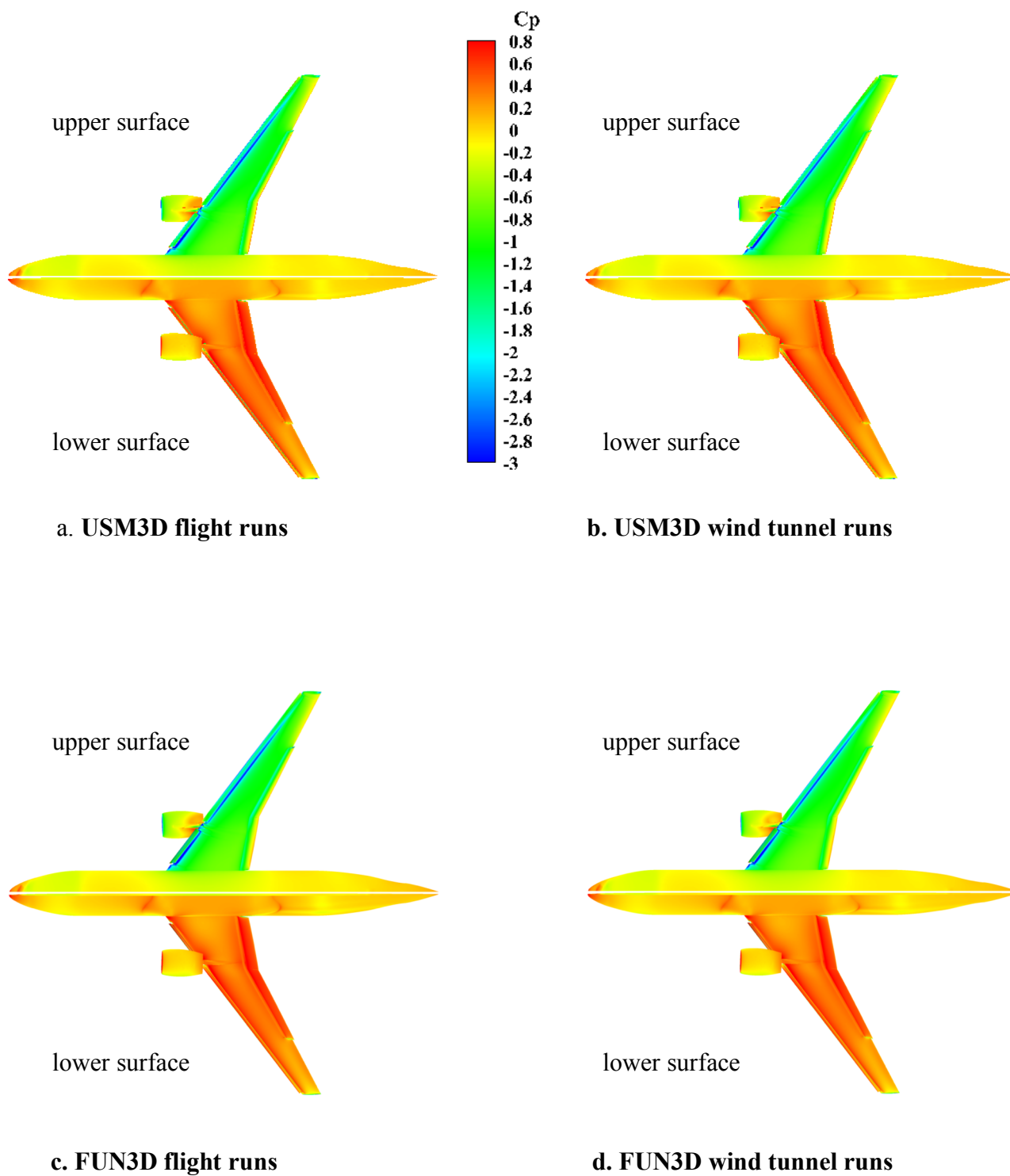


**Figure 26. Takeoff configuration surface pressure distributions,  $\alpha = 8^\circ$ ,  $M=0.26$ ,  $Re=4.24$  million (wind tunnel) and 31.98 million (flight).**

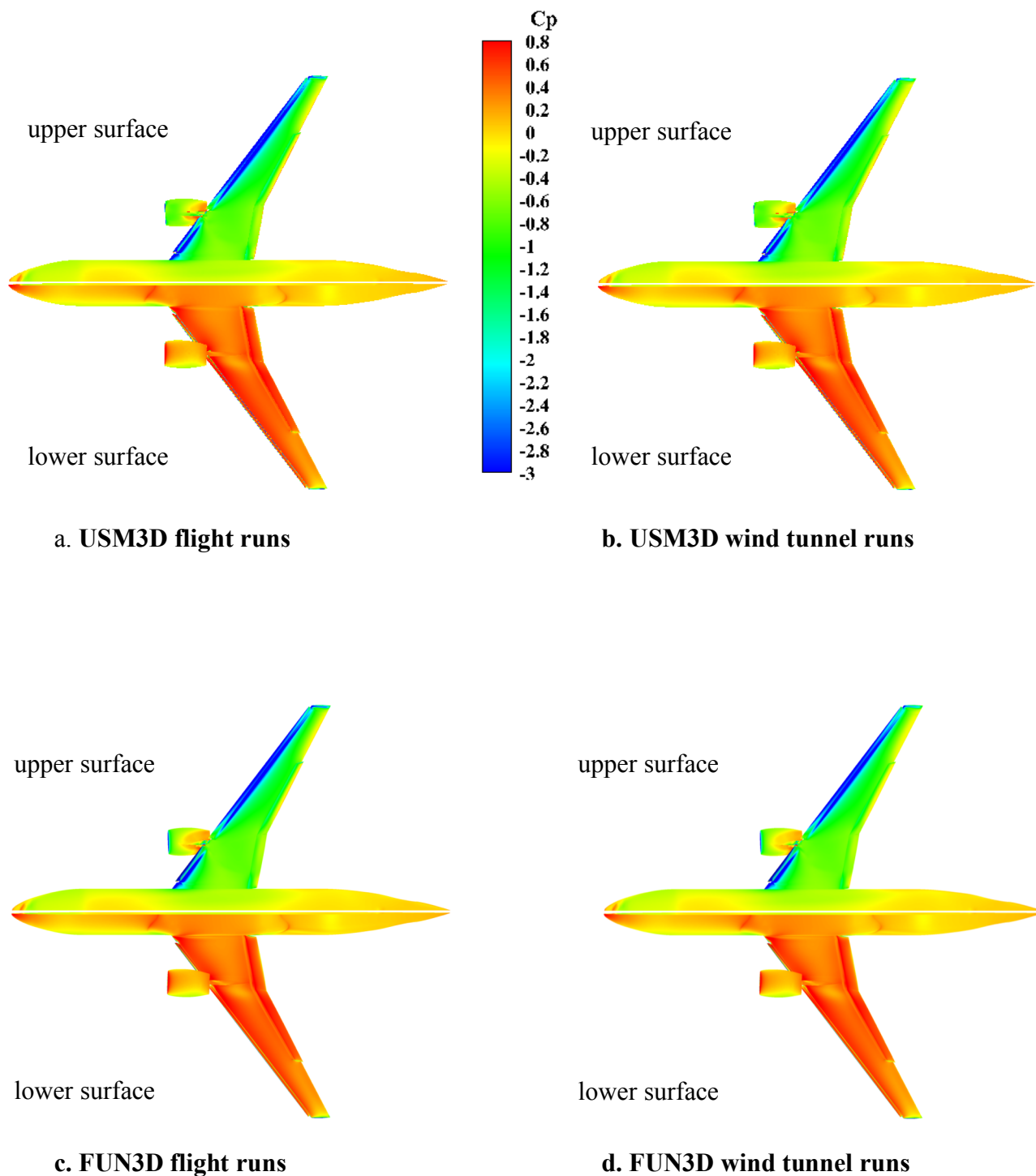


**Figure 27. Takeoff configuration surface pressure distributions,  $\alpha = 16^\circ$ ,  $M=0.26$ ,  $Re=4.24$  million (wind tunnel) and 31.98 million (flight).**